12-1-2014

High-Frequency Gradiometry

Lauren Michelle Kendall

HIGH-FREQUENCY GRADIOMETRY

by

Lauren Michelle Kendall

A Dissertation

Submitted in Partial Fulfillment of the

Requirements for the Degree of

Doctor of Philosophy

Major: Earth Science

The University of Memphis

December 2014

ACKNOWLEDGEMENTS

I would like to thank my advisor, Chuck Langston, for his support and patience throughout this research. He continually challenged me with new ideas, and I appreciate his encouragement. I would also like to thank my committee members for their time and help with this dissertation: Christine Powell, Bob Smalley, Eunseo Choi, and Joan Schmelz. In addition, I am grateful to the CERI students, faculty, and staff for continual support and help all along the way. The CERI community is very special, and I am grateful to have been a part of it.

This dissertation was completed with the funding support from the Center for Earthquake Research and Information and National Science Foundation grant EAR-1417103. The first manuscript was improved by comments made from two reviewers, the second manuscript used data collected by a group of CERI students in a 2006 class who I would like to thank for their hard work, and the third manuscript used help from Bill Halvorson and Bill Banik from Global Geophysical Services who are gratefully acknowledged. In addition, thank you to Global Geophysical Services for generously collecting the dataset used in the third manuscript, and thank you to Hess Corporation for facilitating the collaboration between Global Geophysical Services and The Center for Earthquake Research and Information.

Finally, I would like to thank my family and friends for their patience and for sticking with me throughout these past four and a half years. My parents have always supported me, and I am very grateful. My husband, Will, has taken this journey with me, and I am so lucky to get to experience his sense of humor and encouragement every day.

PREFACE

This dissertation, High-Frequency Gradiometry, includes three papers.

The first paper, "Comparison of Point and Array-Computed Rotations for the TAIGER Explosions of 4 March 2008," authored by Lauren M. Kendall, Charles A. Langston, W. H. K. Lee, C. J. Lin, and C. C. Liu, was published in the *Journal of Seismology*, 16.4, 733-743, 2012.

The second paper, "Small-Scale Experiments in Seismic-Wave Gradiometry," authored by Lauren M. Kendall and Charles A. Langston, has been submitted for publication to *Geophysics*.

The third paper, "Seismic-Wave Gradiometry with a Dense, 2D Array," authored by Lauren M. Kendall and Charles A. Langston, will be submitted for publication to *Geophysics*.

ABSTRACT

Kendall, Lauren Michelle. Ph.D. The University of Memphis. December, 2014. High-Frequency Gradiometry. Major Professor: Dr. Charles A. Langston.

Part 1: Two large explosions were recorded by a dense array of strong-motion accelerometers and rotational seismometers in northeastern Taiwan. The objective of this experiment was to test the response of the experimental Eentec rotational seismometers against calculated array rotations. Computed array rotation rates are seen to have little variation across the array, but point rotation rate measurements show significant deviations with each other and with the array rotation rates in the range of 3–5 Hz. It is not likely that the differences seen in the point and array-computed rotation rates are due to nonlinear or heterogeneous site conditions under each array element since these effects should also be seen in the acceleration data used to determine rotation rate.

Part 2: Three experiments were performed to investigate whether off-the-shelf geophones and seismographs can be used to perform meaningful gradiometry measurements. A standard linear refraction experiment was performed to investigate the slowness of P and Rayleigh waves from hammer sources to compare with measurements taken from two gradiometer designs. One design consists of four, six-instrument gradiometers in a linear array to test the location abilities of the entire gradiometer array. A second gradiometer experiment involved superimposed cells to explore precision in calculation of spatial gradients. We conclude that off-the-shelf equipment can be used to construct small, dense gradiometer arrays.

Part 3: Data from a dense array in Belmont County, Ohio were analyzed with seismic-wave gradiometry techniques in an effort to directly image structure associated with mined areas under the array. In particular, work concentrated on examining how

two of the wave parameters, phase slowness and propagation azimuth, varied with position in the array. The parameters are found to be locally inconsistent when comparing shots of varying azimuths, but they are similar for shots at the same distance and azimuth, indicating a great deal of wave scattering within and outside of the dense array deployment. It is difficult to ascribe phase velocity or wave propagation azimuth directly to structure under small gradiometers.

TABLE OF CONTENTS

LIST OF FIGURES

CHAPTER 1

INTRODUCTION

This dissertation presents three studies using spatial-gradient and wave-gradiometry analysis on data collected using high-frequency sources in Taiwan, Tennessee, and Ohio. Estimating spatial gradients and using the spatial gradients to obtain wave parameters such as phase slowness, propagation azimuth, geometrical spreading, and radiation pattern are valuable tools that allow us to learn more about how the waves propagate from one point to another. Spatial gradient analysis models the wavefield through a Taylor's expansion (Spudich et al., 1995) and exploits the differences between waves. Rotational rate is a product of that analysis when the correct components are combined, and this technique will be used in Chapter 2 to analyze an explosion dataset. We can also use the spatial gradients in conjunction with the displacement and velocity functions at a station to obtain important wave parameters, and this application will be discussed in Chapters 3 and 4 with two different dense datasets. Spatial gradient analysis and wave gradiometry have been applied in the past to a variety of datasets including: earthquake data to calibrate strainmeter instruments with spatial gradients (Grant, 2010), earthquake data from the 2007 Solomon island event recorded in southern California to compute horizontal strains and rotations (Langston and Liang, 2008), strong-motion explosion data with a linear seismic array analyzed using one-dimensional wave gradiometry (Langston, 2007a and 2007c), Rayleigh waves from earthquake data at 400 USArray stations analyzed with two-dimensional wave gradiometry (Liang and Langston, 2009), explosion data from Taiwan analyzed using wave gradiometry (Langston et al., 2009), and local earthquake data from an array in

Moscow, TN analyzed with two-dimensional wave gradiometry (Langston, 2007b). Although the theory has been applied in many settings, the three datasets introduced and analyzed in this dissertation show the analysis with a relatively new type of data. Chapters 2, 3 and 4 show how to approach and analyze these high-frequency, close-proximity datasets with spatial gradient analysis and wave gradiometry.

Comparison of Point and Array-Computed Rotations for the TAIGER Explosions of 4 March 2008

In Chapter 2, explosion data are examined using both accelerometers and rotational seismometers. Eleven accelerometers are combined to make five gradiometer cells. The data from these five cells are analyzed using spatial gradient analysis to produce spatial gradients for the three components of data. These gradients are combined to give rotation at the reference station in the cell, and this rotation estimate is compared against the data from rotational seismometers at the same five stations. We show that the computed rotational waveforms are more correlated in phase and amplitude than the point rotations. To correct the differences, we calculate an amplitude variation, and this correction produces point rotation waveforms that are more similar to the calculated rotation waveforms, but there are still differences. Finally, spectral amplitudes are computed for the point versus computed rotations that illuminate a peak at 4.0 to 4.3 Hz. We conclude that differences in rotation estimates are not due to local site conditions but are more likely due to an instrument response problem with the rotational seismometers. More rigorous tests are needed before the rotational seismometer measurements can be trusted. A huddle test with a known input could be a good place to start.

Small-Scale Experiments in Seismic-Wave Gradiometry

Chapter 3 introduces a dataset collected by a seminar class in 2006 in Memphis, Tennessee. Hammer sources were used to generate signals for this dataset, and off-the-shelf geophones were placed in three distinct configurations to test wave gradiometry with these high-frequency sources. The geophones were first placed in a huddle configuration to find any obvious instrument malfunctions and to attempt to calibrate the instruments. Although this was not possible to do because of geophone-ground interaction, we show that the 4.5% error introduced does not unduly affect the wave gradiometry results. Experiment 1 was a P-wave refraction line with the goal to identify the types of waves present and provide baseline data on velocity structure. The goal of Experiment 2 was to use the compound gradiometer to investigate slowness and azimuth changes over the length of the array, and to test the location abilities of the array. Experiment 3 was designed around a redundant gradiometer layout to investigate wave attribute precision versus number of center stations used in the calculations. We found that the velocities from Experiments 2 and 3 agreed with those found in Experiment 1. In addition, we found that the Experiment 2 array can be used to locate the source, and the Experiment 3 wave-attribute precision increased with more center stations in the array.

Seismic-Wave Gradiometry with a Dense, 2D Array

Chapter 4 involves a 3D industry seismic experiment in Belmont County, Ohio. One kg dynamite sources of varying azimuths and distances were recorded by a 376-station array with dense spacing. New methods of wave gradiometry are introduced to minimize the effects of instrumental amplitude recording statics and to display the phase slowness and propagation azimuth results across the array. The wave gradiometry results

were found to be azimuthally inconsistent which indicated a great deal of scattering within and outside of the array. These results are compared against frequency-wavenumber spectra to show that the two processing techniques produced comparable answers for the dispersion of slowness and azimuth estimates.

CHAPTER 2

COMPARISON OF POINT AND ARRAY-COMPUTED ROTATIONS FOR THE TAIGER EXPLOSIONS OF 4 MARCH 2008

Introduction

Rotational seismology is an emerging field (Lee et al. 2009a, b; Stupazzini et al. 2009). A particular concern is being able to measure rotation rates directly. This has been attempted using instruments such as solid-state devices and ring lasers (e.g., Nigbor 1994; Takeo 1998; Schreiber et al. 2009). Recently, more affordable commercial rotational seismometers have become available that can measure with great sensitivity rotational waves produced from earthquakes, explosions, and other energy sources. In order to effectively use these new instruments, further tests are required by the seismological community to evaluate their accuracy. In this paper, we examine the response of the Eentec R-1 rotational seismometer under field conditions that include recording strong ground motions from nearby large explosions. Others have examined the response of Eentec R-1 rotational seismometers in the laboratory (Nigbor et al. 2009; Wassermann et al. 2009), but not under field conditions that include siting and installation variables. We will examine seismic waves recorded by the Eentec R-1 rotational seismometer and compare them to rotation rates calculated using seismic array "geodesy" (Gomberg et al. 1999) to determine the accuracy of the rotational seismometers. The data come from two large explosions detonated for the Taiwan Integrated Geodynamics Research (TAIGER) (Lin et al. 2009) project in Taiwan on 4 March 2008.

Acceleration data from a dense array of accelerometers are used to calculate wave

spatial gradients and resulting rotation and strain rates (Langston and Liang 2008). Langston et al. (2009) used these methods to examine rotation rate as well as strain rate, wave speed, direction, spatial amplitude variation, and stress for the two large TAIGER explosions although they only examined the vertical component of rotation rate (around the local z-axis). In this article, we will compute all three components of rotation rate (local x, y, and z) compared to the three component rotational velocity data recorded by the Eentec rotational seismometers.

The two TAIGER explosions were detonated about 500 m from the center of the small array (Fig. 1). These explosions, N3P and N3, contained 3,000 and 750 kg of explosives, respectively. Accelerometers and rotational seismometers were positioned close together with 5 m between stations. We will focus on the comparison of each component of rotation rate (or velocity) at each of the five center array stations. There will be 15 waveforms from the rotational seismometers (which will be termed "point rotation rate measurements") and 15 waveforms from array geodesy calculations using data from the accelerometers (which will be termed "array-computed rotation rates") for each of the two explosions for a total of 30 waveforms of each type.

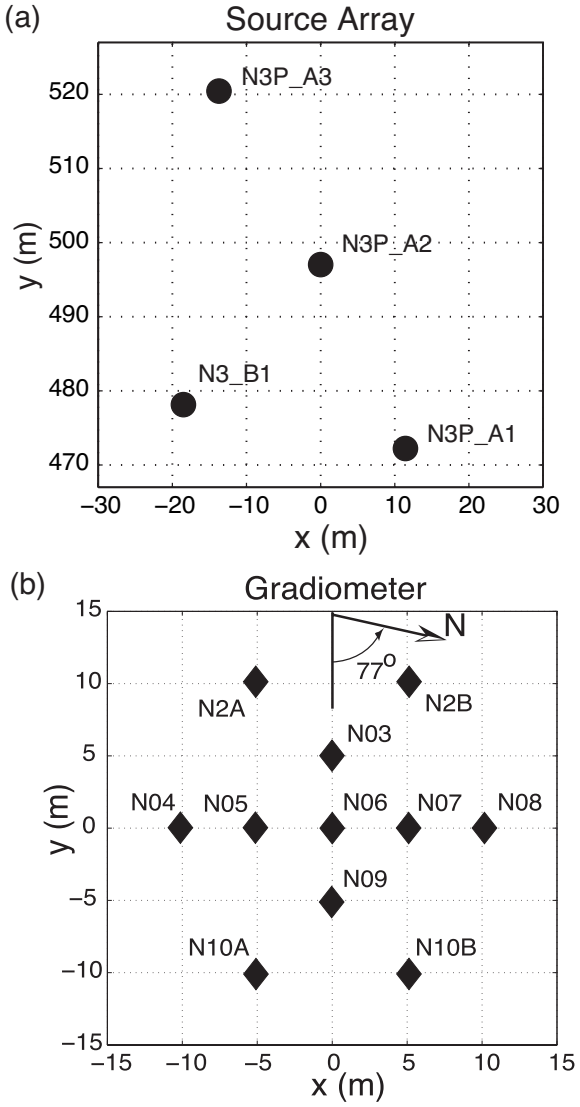

Figure 1: Source and gradiometer geometry
Source (a) and gradiometer (b) geometry from Lin et al. (2009). Borehole locations for the N3P and N3 explosions are labeled in (a) where N3P_A3, N3P_A2, and N3P_A1 correspond to the N3P explosion and N3_B1 corresponds to the N3 explosion. Stations are labeled in (b); we compared rotational waveforms from stations N03, N05, N06, N07, and N09 as they had both a rotational seismometer and an acceleration sensor. Acceleration data from the 11 stations were used to calculate the computed array rotation rates. The direction of positive rotation rate is found using the nontraditional left-handed coordinate system around each of the positive axes (the superimposed Cartesian coordinate system of x, y, and z where z is out of the page and station N06 is the center)

The Eentec R-1 rotational seismometer uses a nontraditional left-handed coordinate system for the direction of positive rotation rate. Referring to Fig. 1, our Cartesian coordinate system follows the general right-handed rule, but the direction of positive rotation about the Cartesian axes as recorded by the rotational seismometers follows a left-handed rule. We adopted this convention to make the comparison between point and array-computed rotation rates. We show that the point rotation rate measurements are variable when compared with the computed array rotation rates. The computed array rotation rates are highly correlated with themselves when compared by component, but the point rotation rate measurements are less correlated with the local x components having the most variations. Reasons for this result are investigated by comparing results for the two different explosions and through Fourier analysis.

Data

The experimental details, setup, and specific calibrations of the TAIGER explosions and of the instrument network are outlined in Lin et al. (2009). Two large explosions were detonated about an hour apart on 4 March 2008; the first one consisted of three simultaneous 1,000 kg borehole explosions (known as N3P) and was detonated at 17:01 UT, and the second explosion contained 750 kg of explosives in one single borehole (known as N3) and was detonated at 18:01 UT. For simplicity, a Cartesian coordinate system is centered at station N06 (Fig. 1) with the middle borehole of the N3P explosion situated about 500 m from the center of the instrument array. Instrument locations N03, N05, N06, N07, and N09 contain both accelerometers and rotational seismometers and are the stations of interest in comparing the two data sets. However, all 11 stations contain accelerometers and each accelerograph of the array is used to compute

rotation rates for the five, inner array elements. The array was specifically designed to sample less than 10 % of the target wavelength to accurately compute the wave spatial gradients (Langston et al. 2009). Seven of the stations had Metrozet TSA-100S acceleration sensors and the others had Kinemetrics Episensor ES-T sensors. The five center array elements also had Eentec R-1 rotational seismometers with Quanterra Q330 dataloggers. The two types of accelerometers are both force-balanced, and their amplitude responses are flat from 0 to 225 and 200 Hz, respectively (Lin et al. 2009). Factory specifications for the instruments and on-site calibrations are presented in Lin et al. (2009).

Theoretical Background

Rotation rate is computed using wave spatial gradients obtained from observation of accelerations at each station in the array. The spatial gradients are found by modeling the wavefield through a Taylor's expansion as suggested by Spudich et al. (1995). This process is applied to the acceleration data in order to compute rotation acceleration for each of the three components at each of the five stations and then integrating to obtain rotation rate.

The rotation rate can be computed by first relating it to an incoming wave through its spatial gradient. Rotation rate is calculated relative to a reference point or 'master receiver,' which will be the locations of each accelerometer at stations N03, N05, N06, N07, and N09. The spatial gradient at the master receiver (s_0) can be related to the wavefield at all other receivers (s_i) (Langston and Liang 2008; Liang and Langston 2009):

$$du_i = u_i - u_0 = \delta x_i \left.\frac{\partial u}{\partial x}\right|_{S_0} + \delta y_i \left.\frac{\partial u}{\partial y}\right|_{S_0} + du_i^{err} \tag{1}$$

where i=1,2,...,N where N is the number of stations, u can be u_x, u_y, or u_z, and $\delta x_i = x_i - x_0$ and $\delta y_i = y_i - y_0$. We are using the assumption that the error, du_i^{err}, is of second order and can be neglected. In matrix form:

$$\mathbf{Gm} = \mathbf{d} \tag{2}$$

where,

$$\mathbf{G} = \begin{bmatrix} \delta x_1 & \delta y_1 \\ \delta x_2 & \delta y_2 \\ \vdots & \vdots \\ \delta x_N & \delta y_N \end{bmatrix}$$

$$\mathbf{m} = \begin{bmatrix} \left.\frac{\partial u}{\partial x}\right|_{S_0} \\ \left.\frac{\partial u}{\partial y}\right|_{S_0} \end{bmatrix}$$

$$\mathbf{d} = \begin{bmatrix} du_1 \\ du_2 \\ \vdots \\ du_N \end{bmatrix} \tag{3}$$

The least-squares solution for the spatial gradients is:

$$\mathbf{m} = (\mathbf{G}^T\mathbf{G})^{-1}\mathbf{G}^T\mathbf{d}. \tag{4}$$

The three components of rotation rate about the x, y, and z axes at the Earth's surface are (Lin et al. 2009):

$$\omega_x = \frac{\partial u_z}{\partial y}$$

$$\omega_y = -\frac{\partial u_z}{\partial x}$$

$$\omega_z = -\frac{1}{2}\left(\frac{\partial u_x}{\partial y} - \frac{\partial u_y}{\partial x}\right) \quad (5)$$

Inserting the proper component of the spatial gradient into equation (5) gives the rotation rate about each axis.

Data Analysis

Units for observed rotation rates are in milliradians per second. The derived array rotation rates start from differencing acceleration using the theory listed in the previous section, in centimeters per square second to obtain radians per square second. The original acceleration records are presented in Langston et al. (2009) in the bands 3–5 and 3–50 Hz. Langston (2007) provides a discussion on the error level associated with calculating spatial derivatives. Rotation acceleration is then time-integrated to obtain rotation rate using the Fourier integral theorem and then scaled to obtain milliradians per second. We then convolved the nominal Eentec R-1 rotational sensor instrument response into the computed array rotations to compare them with the point rotation rate data. We also applied a 3–5 Hz frequency bandpass filter after multiplying them by negative one to account for the nontraditional direction of positive rotation.

Ideally, the point rotation rate measurements should be identical to the computed

array rotation rates as they both are recordings of the rotational waves from the two large explosions. The rotation rates at each of the five stations should have the same shape because the horizontal seismic wavelength in our assumed bandpass is greater than the array aperture of 10 m. For example, a 4-Hz P wave with a horizontal phase velocity of 4,000 m/s would have a horizontal wavelength of 1,000 m which is much greater than the array diameter (Langston et al. 2009). This is the reason for choosing the 3–5 Hz bandpass. This relatively low frequency bandpass is well within the responses of both the accelerometers and the Eentec R-1 rotational seismometer while preserving the requirement that the array aperture be 10 % or less than the observed seismic wavelengths.

Point and array rotation rates were plotted by explosion (N3P and N3) and then by the local *x*-, *y*-, and *z*-axes (Fig. 2). The point rotation rate measurements have noticeable amplitude and phase differences. The superimposed computed array rotation rates, on the other hand, show very little variation. This indicates two things: First, the array-computed rotation rates are quite stable because they show almost no variation over the array. This consistency of rotation rate estimates, even using different reference points for the Taylor series inversion, is consistent with the expected wave propagation. Long-wavelength seismic waves should not change amplitude or phase over relatively short distance ranges. Secondly, but much more problematical, the rotational sensor waveforms have small time shifts and amplitude variations among themselves and when compared to the "correct" array-derived rotation rates. Largest waveform variations occur for the *x* components of stations N06 and N09.

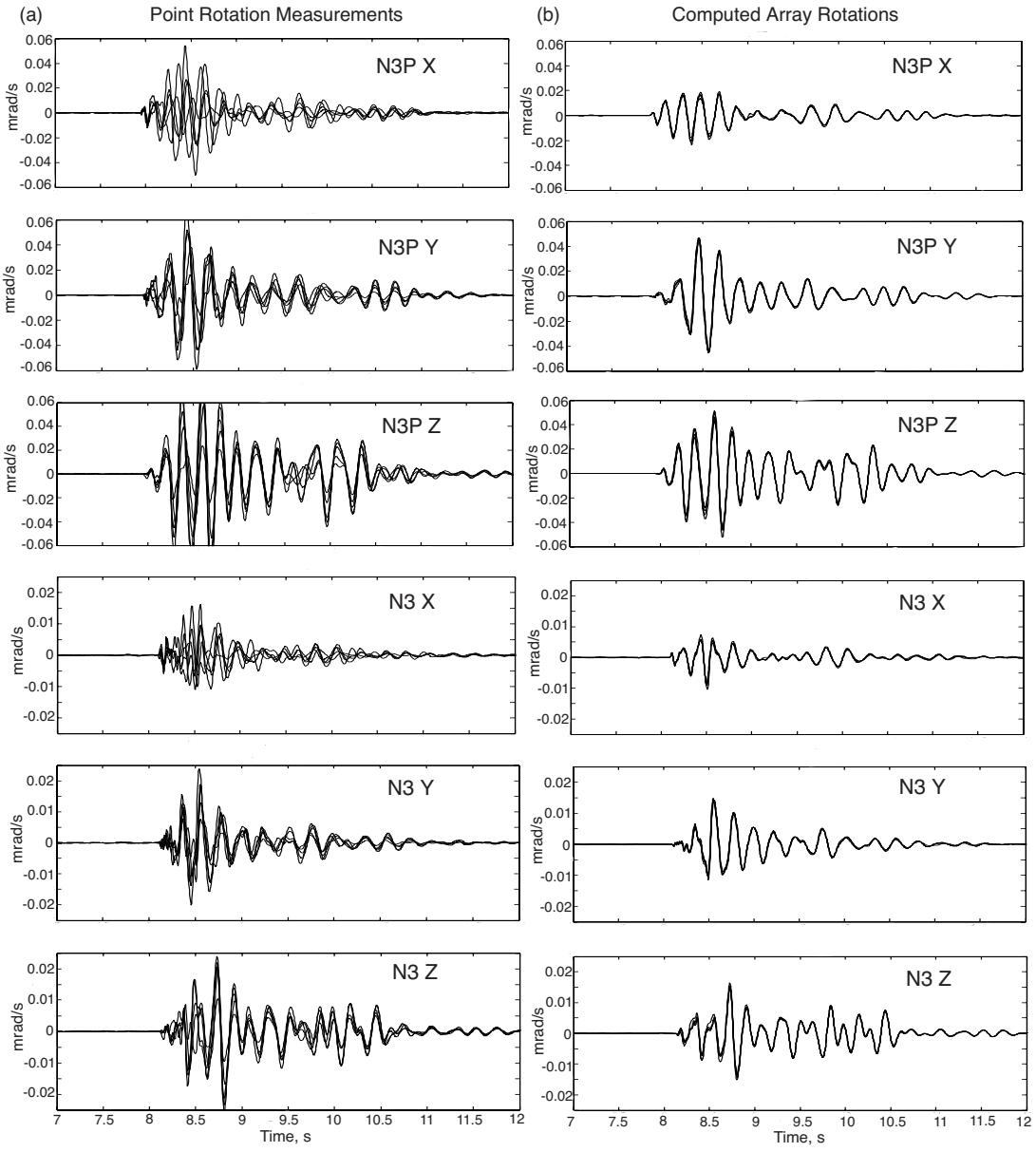

Figure 2: Rotation waveforms filtered 3-5 Hz
Local *x*, *y*, and *z* components of rotation rate for each of the explosions with the measurements at the five stations superimposed in the frequency range 3–5 Hz. Point rotation rate measurements (a) show considerable variations and are distinguishable from each other while the computed array rotation rates (b) show such little variation that the five waveforms plotted are almost indistinguishable

In an attempt to quantify the differences in the point rotation rate measurements, cross-correlation of the point and array rotation rates was applied to the filtered waveforms for each component of each station. We were interested in waveform similarity, given by the maximum of the normalized cross-correlation, the time shift that gave the maximum normalized cross-correlation, and the amplitude of the un-normalized cross-correlation at zero time shift (Table 1). The absolute values of the normalized cross-correlation coefficients range from 0.45 to 0.97 with an average of 0.84. The optimum, least-squares estimate of the amplitude variation of the un-normalized cross-correlations is represented by:

$$A = \frac{[O(t) \otimes S(t)]_{\tau=0}}{[S(t) \otimes S(t)]_{\tau=0}} \quad (6)$$

where the circled cross denotes the cross-correlation, *O(t)* is the point rotation rate measurement, and *S(t)* is the computed array rotation rate (Langston et al. 2002).

Our first comparison was to simply divide each point rotation rate measurement by its inferred amplitude variation value. The new, "corrected" waveforms were then superimposed on the computed array rotation rates (Fig. 3). With these corrections, the waveforms become more similar for the *y* and *z* components, but the *x* component waveforms still vary wildly.

Table 1: Quantifying waveform similarity
This table presents a quantifiable comparison of the rotation rate waveforms of each component and explosion using normalized maximum cross correlations and amplitude variations. The lag at the maximum normalized cross correlation gives the time shift of the waveforms.

Explosion N3P				Explosion N3			
Station + Component	Norm. Max. Cross Corr. Coeff.	Lag at Max. Cross Correlation Coefficient (s)	Amplitude Ratio at Zero Lag	Station + Component	Norm. Max. Cross Corr. Coeff.	Lag at Max. Cross Correlation Coefficient (s)	Amplitude Ratio at Zero Lag
3 X	0.92	-0.02	0.86	3 X	0.84	0.00	0.91
3 Y	0.97	0.02	0.73	3 Y	0.94	0.00	0.94
3 Z	0.94	0.01	1.41	3 Z	0.85	0.01	1.24
5 X	0.88	-0.04	0.89	5 X	-0.74	-0.13	0.81
5 Y	-0.89	-0.12	1.22	5 Y	-0.86	-0.12	1.15
5 Z	0.85	0.01	0.53	5 Z	0.84	0.01	0.60
6 X	-0.60	0.21	-0.99	6 X	0.45	-0.10	-0.47
6 Y	0.76	0.01	0.35	6 Y	0.83	0.01	0.45
6 Z	0.95	0.01	1.81	6 Z	0.88	0.01	1.37
7 X	0.82	-0.02	0.70	7 X	-0.76	0.07	0.62
7 Y	-0.92	-0.12	1.01	7 Y	0.85	0.00	0.89
7 Z	0.95	0.02	1.03	7 Z	0.89	0.01	0.97
9 X	-0.77	-0.07	0.26	9 X	0.70	0.03	0.22
9 Y	-0.93	-0.11	1.06	9 Y	-0.88	-0.11	1.00
9 Z	0.93	0.00	1.46	9 Z	0.87	0.01	1.22

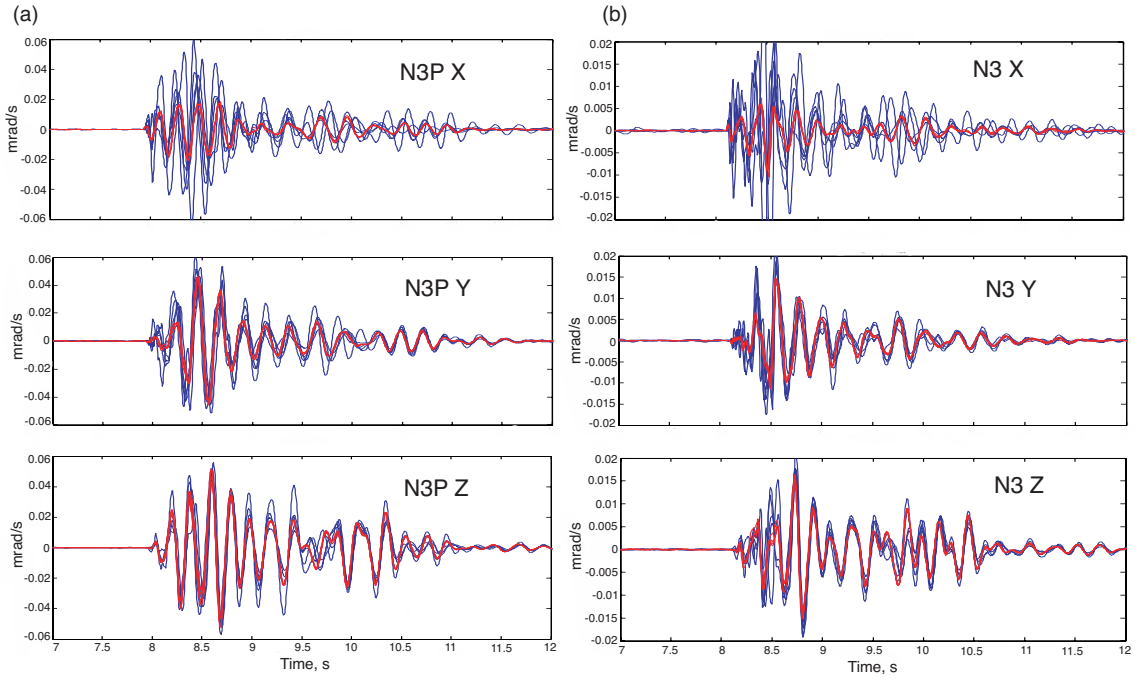

Figure 3: Corrected and computed rotation rates
Superimposed corrected point rotation rate measurements (corrected by dividing the original point rotation rate measurements by the amplitude ratio value from Table 1) and computed array rotation rates for explosion N3P (**a**) and explosion N3 (**b**). The blue waveforms are the corrected point rotation rate measurements, and the red waveforms are the computed array rotation rates. Notice the similarities of the *y* and *z* components and the wild amplitude variations of the *x* component waveforms, specifically at stations N06 and N09

We then investigated spectral amplitude ratios of the observed point rotation rates compared to the array rotation rates to see if there were consistent characteristics that could be attributed to differences in spectral instrument response among the rotational seismometer channels. First, all of the waveforms were transformed into the frequency domain using an FFT. The number of points in the time series is 6001, so the corresponding frequency resolution is 0.03 Hz. The amplitude spectra were smoothed using a running average of 10 points (or 0.3 Hz) on either side of the center frequency (Fig. 4) in order to avoid irregularities and zeros, which would cause spectral ratios to have spurious peaks. After smoothing, spectral ratios of the point to array rotation rates for each component of each station were computed (Fig. 5).

Most *z* channels show a resonance peak at about 4.1 Hz that can increase observed rotation rate amplitudes by factors of 2 to 4 (Fig. 5). *Y* channels seem best behaved with more subdued resonance peaks and spectra that suggest a response within 50 % of advertised values. *X* channels show the greatest variation in spectral ratios with the appearance of large resonance peaks near 4.3 Hz that amplify rotational motions by up to factors of 10. Notably, station 3 *x* component spectral ratios are comparable to the better *y* components. Spectral ratios for each event are similar, but the smaller explosion, N3, seems to have greater resonance peaks than the larger explosion, N3P.

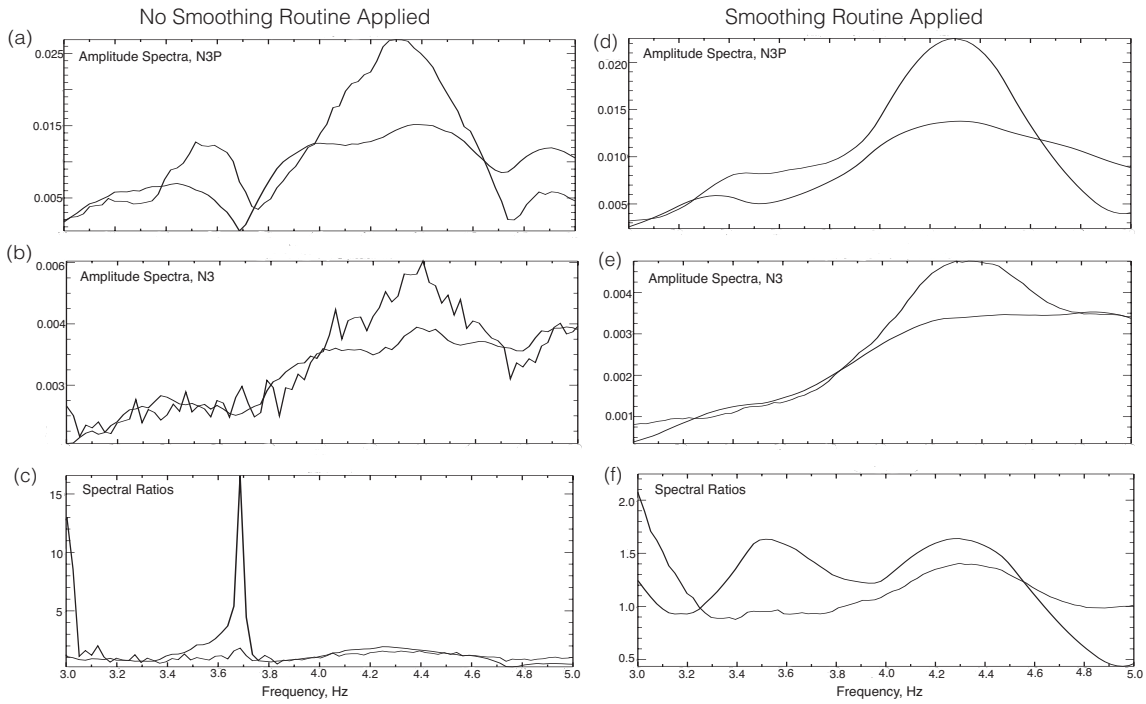

Figure 4: Smoothed and unsmoothed spectral ratios
Component *y* from station N06 is shown to illustrate the benefit of using a smoothing operator. For this figure and Fig. 5, a running average of ten points on either side of the center frequency was applied (Goldstein et al. 2003). Amplitude spectra (**a**, **b**, **d**, **e**) are shown with (*right-handed column*) and without (*left-handed column*) smoothing applied where the *thick lines* are the array-computed rotation rates and the *thin lines* are the point rotation rate measurements. Notice how a smoothing routine filters out the discontinuities. The spectral ratios (**c**, **f**) are shown with and without smoothing where the *thick line* represents explosion N3P and the *thin line* represents explosion N3. The spectral ratios were calculated with the point rotation rate measurements divided by the array-computed rotation rates

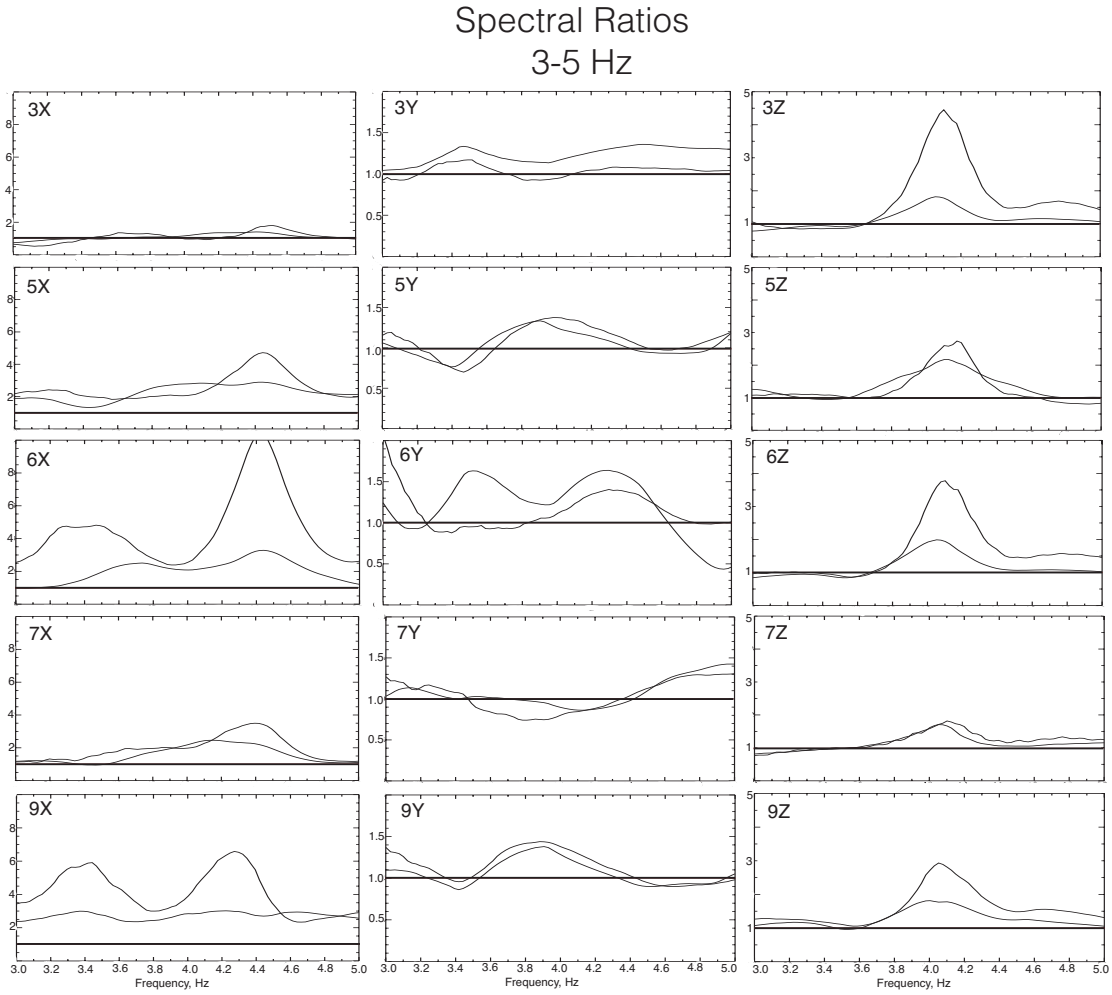

Figure 5: Spectral ratios 3-5 Hz
Unit-less spectral ratios of the point rotation rate measurements to the array-computed rotation rates for each explosion at each of the five stations in the range of 3–5 Hz. Each plot contains the spectral ratio from both explosions and is separated by station component. The *thicker line* is for the N3P explosion and the *thinner line* for the N3 explosion. The *horizontal line* denotes a ratio of one. Note that the amplitude scale is the same for each component but changes between components

Discussion

A field experiment of this type potentially contains many more variables that may affect seismic recordings than would normally occur in more controlled laboratory conditions. It is natural to suspect that very local site and wave coupling conditions under each instrument could affect both the acceleration and rotation rate measurements. The experiment was performed in the Lan-Yang river valley with hills, roads, and a cultivated field nearby (Lin et al. 2009). Photographs of individual array elements show that concrete pads were poured over a heterogeneous mix of river gravels and large cobbles. Perhaps this kind of site heterogeneity gave rise to very local wave scattering, base resonance, or some other unknown, nonlinear condition to cause substantial variations between rotational seismometer recordings.

The Eentec rotational sensors themselves were tested before the experiment, and the sensitivity values obtained were off by as much as 30 % from the factory specifications (Lin et al. 2009). However, the method used was approximate; Lin et al. (2009) states that "…this method determines the average sensitivity over several frequency bands, so that the total frequency response cannot be obtained." Nominally, the response of the Eentec R-1 is flat to rotation rate between 0.05 and 20 Hz. The data comparisons of Figs. 2, 3, and 5 show that there is considerable variation among the rotation channels of the array. What is the most likely source of these variations?

The array accelerations offer a strong clue. The wavefield in the 3–5-Hz frequency band is very consistent over all elements of the strong-motion array (Langston et al. 2009). Furthermore, the computed array rotation rates using the geodetic technique are equally consistent over each rotation element of the array (Fig. 2). If there were some

local site resonance or nonlinear effect at each station of the array, these effects should be seen in causing variation among the computed array rotation rates. Instead, both the accelerations and array rotation rates show what would be expected if ground motions are sampled over distance scales much less than a seismic wavelength. Even in the presence of site heterogeneity, the horizontal seismic wavelengths are simply too large to detect small-scale heterogeneity of a few meters or less. The acceleration and array rotation rate data are consistent with long-wavelength wave propagation.

For completeness, we also applied a 3–50 Hz frequency bandpass filter to the rotation rate data to show the high frequency component of the waveforms (Fig. 6). This gave the results that we expected: The waveforms are less correlated in the higher band than in the 3–5 Hz range. This is because the waves included in the 3–50 Hz band are shorter period, so the original requirement that the array aperture sample less than 10 % of a wavelength is not honored. The point rotation rate measurements show large amounts of variability within the small time window of 0.4 s in Fig. 6. This is the reason the 3–5 Hz bandpass frequency was used in the analysis of this paper: The waves being sampled are greater than ten times the array aperture, so the array-computed waveform calculations are accurate, and they can be correctly compared to the point rotation rate waveforms.

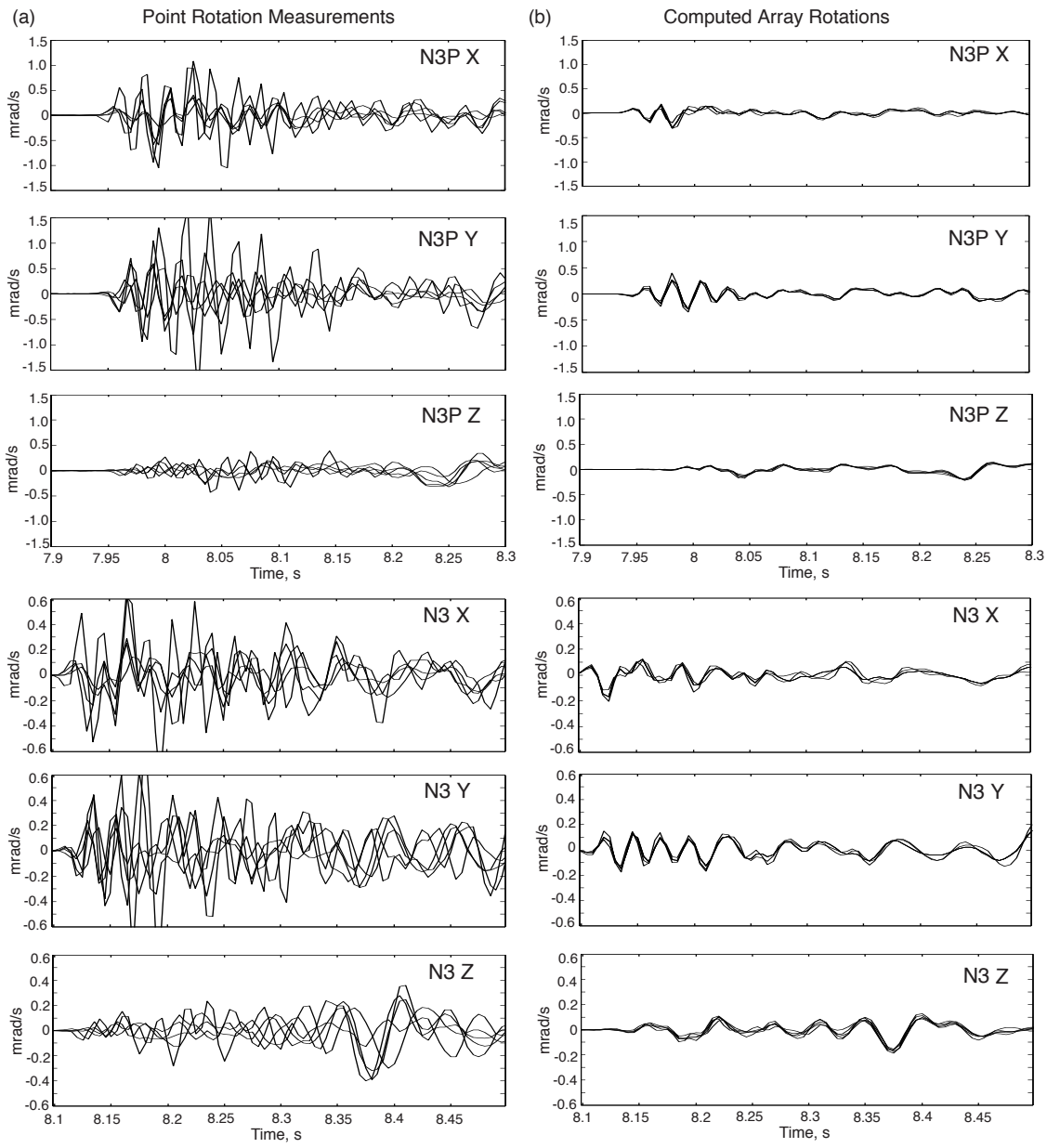

Figure 6: Rotation waveforms filtered 3-50 Hz
Local *x*, *y*, and *z* components of rotation rate in the 3–50-Hz range with the five waveforms at each station superimposed. The waves shown are the first 0.4 s of motion, and there is a change in the times from the N3P to N3 explosions. The point rotation rate measurements (**a**) show large variations with one another—even more than in Fig. 2. The array-computed rotation rates (**b**) show more variations with each other compared to the low frequency bandpass because these short period waves have wavelengths that are less than ten times the array aperture, which increases the error in computed array rotation rates

We considered the effect that rotation could have on the acceleration recordings themselves to estimate any bias that might occur in using acceleration data contaminated with tilts and rotations. It is well-known that horizontal seismographs are sensitive tilt meters. Horizontal component strong-motion accelerometers will be directly affected by a component of gravity through $g\Theta$ where g is the gravitational acceleration and $\Theta \ll 1$ is the tilt or rotation about a perpendicular horizontal axis. However, the horizontal rotations are functions of the vertical acceleration through Eq. (5). Vertical acceleration is insensitive to tilt, to first order but would be more sensitive to contamination with a small component of horizontal acceleration being detected by the tilted vertical accelerometer. However, the largest rotation rates are of the order of 1 mrad/s which would only cause a contamination of approximately 0.1 % in cross axis ground motion. Furthermore, Grazier (2005) showed that within a limited frequency band, the long-period errors introduced by tilting are eliminated.

Both the variation in waveform and variation in spectral characteristics among the channels of the rotational seismometer array strongly suggest that the variation is due to variations in the instrument responses (Figs. 2, 3, and 5). The x and z component data show similar spectral resonances near 4.0–4.3 Hz for both explosion sources. It is also interesting to observe that spectral ratio data for the smaller event that occurred 1 h after the large explosion show higher amplitude ratios with the array-computed rotation rates. Perhaps the sensors sustained mild damage during the large explosion. Investigating these conjectures is beyond the purpose of this report.

Another reason for the waveform variation that needs to be explored in future studies is amplitude distortion. The output response we are analyzing in this paper could

be a nonlinear function of the input wave amplitude. If these were the case, just removing the linear instrument response would not fix the variations seen in the point rotation rate measurements. Investigating nonlinearity requires controlled input signals where amplitude and signal phase can be varied to explore the resulting output. It has been suggested that there might be distortion effects in the rotational seismometers that starts at 20–40 % of full scale (Nigbor, personal communication, November 12, 2011). The clip level of the rotational seismometers is 1 rad/s at 1 Hz (Eentec specification sheet). The waveforms shown in this paper have amplitudes of up to 1.5 mrad/s which is only 1.5 % of full scale, far from 20 % to 40 % of the maximum output of the instrument.

After correction by the inferred amplitude ratio found from the zero-lag cross-correlation (Table 1), the point data waveforms generally agree with the array rotation rates, except for the *x* components at stations N06 and N09 (Fig. 3). This suggests that a rigorous testing program is required before fielding these instruments to determine more accurate instrument responses. One such method might involve a long-duration "huddle" test where instruments are grouped closely to each other on a solid pad. Recordings of high amplitude ambient noise could be used to determine accurate relative rotation rate responses using techniques suggested by Pavlis and Vernon (1994).

Conclusions

Acceleration-derived geodetic rotation rates and point rotation rate data recorded by Eentec R-1 rotational seismometers after two large explosions in northeastern Taiwan were successfully compared. Computed array rotation rate showed little variation over the five array stations, consistent with long-wavelength seismic wave propagation. However, the point rotation rate measurements showed considerably more variation

among themselves and when compared to the array rotation rates quantified by normalized cross-correlation coefficients, amplitude variation at zero cross-correlation lag (Table 1), and ratios of the spectra of point to array rotation rates.

The absolute value of the normalized cross-correlation values between the two sets of rotational waveforms in the frequency band 3–5 Hz had an average of 0.84. Spectral analysis showed that the spectral ratios varied by component and often had large resonance peaks near 4.0–4.3 Hz. The *x* components of two stations (N06 and N09) were particularly problematical. Variations in the observed point rotation rate data are attributed to variations in instrument response and not site heterogeneity.

References

Goldstein P, Dodge D, Firpo M, Minner L (2003) SAC2000: signal processing and analysis tools for seismologists and engineers. In: Lee WHK, Kanamori H, Jennings PC, Kisslinger C (eds) The IASPEI international handbook of earthquake and engineering seismology. Academic, London

Gomberg J, Pavlis G, Bodin P (1999) The strain in the array is mainly in the plane (waves below 1 Hz). Bull Seismol Soc Am 89(6):1428–1438

Grazier VM (2005) Effect of tilt on strong motion data processing. Soil Dyn and Earthq Eng 25:197–204

Langston CA (2007) Spatial gradient analysis for linear seismic arrays. Bull Seismol Soc Am 97(1B):265–280

Langston CA, Liang C (2008) Gradiometry for polarized seismic-waves. J Geophys Res 113:B08305

Langston CA, Nyblade AA, Owens TJ (2002) Regional wave propagation in Tanzania, East Africa. J Geophys Res 107:B1. doi:10. 1029/ 2001JB000167

Langston CA, Lee WHK, Lin CJ, Liu CC (2009) Seismic-wave strain, rotation, and gradiometry for the 4 March 2008 TAIGER explosions. Bull Seismol Soc Am 99(2B):1287–1301

Lee WHK, Huang BS, Langston CA, Lin CJ, Liu CC, Shin TC, Teng TL, Wu CF (2009a) Review: progress in rotational ground-motion observations from explosions and local earthquakes in Taiwan. Bull Seismol Soc Am 99(2B):958–967

Lee WHK, Igel H, Trifunac MD (2009b) Recent advances in rotational seismology. Seismol Res Lett 80(3):479–490

Liang C, Langston CA (2009) Wave gradiometry for USArray: Rayleigh waves. J Geophys Res 114. doi:10. 1029/ 2008JB005918

Lin CJ, Liu CC, Lee WHK (2009) Recording rotational and translational ground motions of two TAIGER explosions in northeastern Taiwan on 4 March 2008. Bull Seismol Soc Am 99(2B):1237–1250

Nigbor RL (1994) Six-degree-of-freedom ground-motion measurement. Bull Seismol Soc Am 84(5):1665–1669

Nigbor RL, Evans JR, Hutt CR (2009) Laboratory and field testing of commercial rotational seismometers. Bull Seism Soc Am 99:1215–1227

Nigbor, RL. Letter to the author. November 21, 2011.

Pavlis GL, Vernon FL (1994) Calibration of seismometers using ground noise. Bull Seism Soc Am 84:1243–1255

Schreiber KU, Hautmann JN, Velikoseltsev A, Wassermann J, Igel H, Otero J, Vernon F, Wells JPR (2009) Ring laser measurements of ground rotations for seismology. Bull Seism Soc Am 99:1190–1198

Spudich P, Steck LK, Hellweg M, Fletcher JB, Baker LM (1995) Transient stresses at Parkfield, California, produced by the M 7.4 Landers earthquake of June 28, 1992: observations from the UPSAR dense seismograph array. J Geophys Res 100:675–690

Stupazzini M, Puente J, Smerzini C, Kaser M, Igel H, Castellani A (2009) Study of rotational ground motion in the near-field region. Bull Seismol Soc Am 99(2B):1271–1286

Takeo M (1998) Ground rotational motions recorded in near-source region of earthquakes. Geophys Res Lett 25(6):789–792

Wassermann J, Lehndorfer S, Igel H, Schreiber U (2009) Short note: performance test of a commercial rotational motions sensor. Bull Seismol Soc Am 99(2B):1449–1456

CHAPTER 3

SMALL-SCALE ARRAY EXPERIMENTS IN SEISMIC-WAVE GRADIOMETRY

Introduction

Seismic instruments are positioned in arrays to exploit the normal moveout of seismic phases in order to calculate an estimate of phase velocity and azimuth. These estimates provide information about the wavefield that can be used to answer questions about subsurface properties and presence of reflectors in the wavepath. A common technique to find the phase velocity and azimuth is a stacking method called beamforming. This method essentially smooths the wavefield to increase the signal-to-noise ratio, but the method has a potential drawback: the station spacing must be greater than twice the minimum wavelength (Hinich, 1981). Wave gradiometry is a relatively new array-processing technique that produces phase velocity and azimuth estimates as well as determining amplitude variations with distance and angle (geometrical spreading and radiation pattern, respectively) for an array. Because it requires the station spacing be less than 10% of the minimum wavelength (Langston, 2007b), stations cover less area than beamforming. For high frequency sources used in reflection and refraction studies, wave gradiometry can provide additional information about the wavefield, and the array configuration takes up considerably less surface area while sampling the same wave frequencies.

Seismic-wave gradiometry uses wave displacement observations from a two-dimensional array of stations, called a gradiometer cell, to estimate spatial gradients. Compatibility of the spatial gradients with the original wave field yield wave characteristics of horizontal slowness, propagation azimuth, geometrical spreading

changes, and radiation pattern changes for the localized spot sampled by the cell (Langston, 2007a, 2007b, 2007c). Wave characteristics are unique to structure beneath the stations and to the state of the incident wavefield before interacting with the cell.

In Fall 2006, a graduate seminar class in Geophysics was taught at the University of Memphis where the students built and tested gradiometer arrays with a refraction/reflection seismograph and off-the-shelf vertical geophones. The sources used in these experiments were high frequency hammer blows close to the arrays, which allowed the investigation of highly variable wavefields similar to wavefields used in exploration and reflection seismology. Horizontal slowness and propagation azimuth were estimated using three small-scale arrays to verify that wave gradiometry yields accurate wave characteristics using geophone observations. These arrays consist of a 24-station, linear P-wave refraction line (hereafter called "Experiment 1"), a compound gradiometer ("Experiment 2"), and a redundant gradiometer ("Experiment 3") shown in Figure 7. We will show that the velocities from the refraction line in Experiment 1 agree with Experiments 2 and 3 velocity results. We also will see in Experiment 2 that the cells can be used to locate the source. Experiment 3 will show that when there are more center stations included in the gradiometry calculation, the precision of the horizontal slowness and propagation azimuth calculations increase. The results will show that wave gradiometry wave attributes can be accurately estimated and implemented with off-the-shelf geophones.

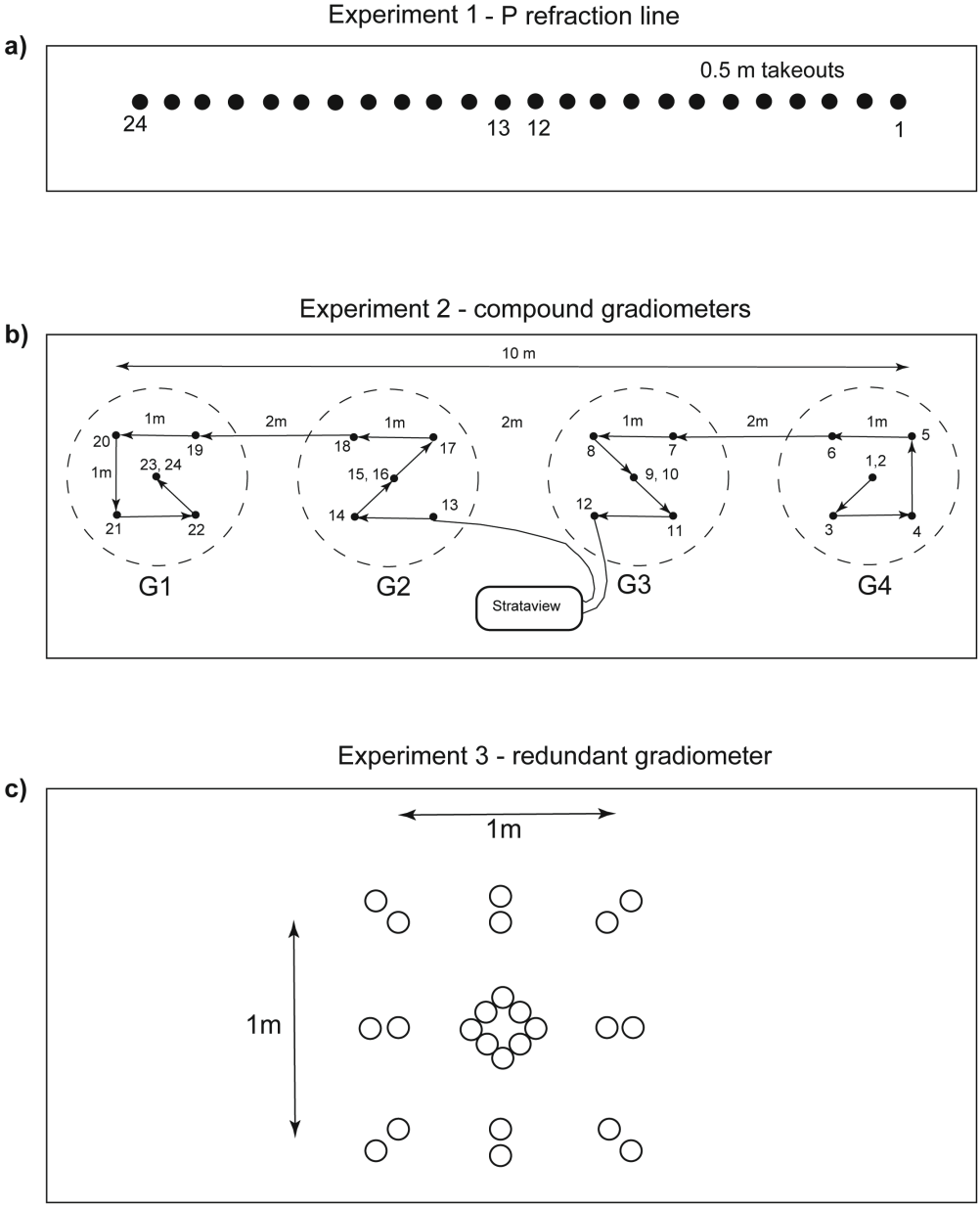

Figure 7: Geophone geometry
Geophone geometry for Experiment 1 (a), Experiment 2 (b), and Experiment 3 (c). Experiment 1 was a P-wave refraction line consisting of 24 vertical geophones with 0.5 m takeouts for a line extent of 11.5 meters. Experiment 2 was made up of four gradiometer cells of six stations each with 0.5 meter station spacing; the total length over the four cells is ten meters. Experiment 3 was a "redundant" gradiometer named for the additional geophones at each outer point and in the center; the total extent of the box is one meter by one meter.

Methods

2D Wave Gradiometry

Array seismic-wave gradiometry is based on the computation of the wave spatial gradient between stations in a dense array where the array is a fraction of a wavelength in aperture compared to the target wavelength. Wave spatial gradients combined with the original wave field and its time derivative yield horizontal slowness, wave-propagation azimuth, geometrical spreading changes, and radiation pattern changes at a reference station in the dense array (Langston, 2007a, 2007b, 2007c). To illustrate the process, we start with a two-dimensional cylindrical wave displacement of the form:

$$u(t,r,\theta) = G_r(r)R(\theta)f(t - p_r(r)(r - r_0)) \tag{7}$$

where $u(t,r,\theta)$ is the wave displacement, $G_r(r)$ is the geometrical spreading, $R(\theta)$ is the radiation pattern, and $p_r(r)$ is the distance-dependent slowness. Differentiating equation 7 with respect to r and θ gives

$$\frac{\partial u(t,r,\theta)}{\partial r} = A_r(r)u(t,r,\theta) + B_r(r)\frac{\partial u(t,r,\theta)}{\partial t} \tag{8}$$

$$\frac{\partial u(t,r,\theta)}{\partial \theta} = \Re(\theta)u(t,r,\theta) \tag{9}$$

where

$$A_r(r) = \frac{G_r'(r)}{G_r(r)} \tag{10}$$

$$B_r(r) = -\left[p_r + \frac{\partial p_r}{\partial r}(r - r_0)\right] \tag{11}$$

and

$$\Re(\theta) = \frac{R'(\theta)}{R(\theta)} \quad . \tag{12}$$

Equations 8 and 9 represent an important relationship between the wave spatial gradient, original wavefield, and its time derivative. Integrating equations 10, 11, and 12 yields the geometrical spreading, horizontal slowness, and radiation pattern of the wave given by

$$\int_{r_0}^{r} A_r(r)dr = ln\frac{G_r(r)}{G_r(r_0)} \tag{13}$$

$$p_r(r) = -\frac{1}{(r-r_0)}\int_{r_0}^{r} B_r(r) \tag{14}$$

and

$$\int_{\theta_0}^{\theta} \Re(\theta)d\theta = ln\frac{R(\theta)}{R(\theta_0)} \quad . \tag{15}$$

To find the coefficients, A_r and B_r, we must first perform two one-dimensional problems in *x* and *y* to find $A_x(x)$, $A_y(y)$, $B_x(x)$, and $B_y(y)$. For example, we can assume the Cartesian displacement in *x* as

$$u(t,x) = G(x)f(t - p(x - x_0)) \tag{16}$$

where $G(x)$ is the geometrical spreading, p is the horizontal wave slowness, and x_0 is the *x* component of the reference station position. Differentiating equation 16 with respect to *x* gives

$$\frac{\partial u}{\partial x} = A_x(x)u + B_x(x)\frac{\partial u}{\partial t} \tag{17}$$

where

$$A_x(x) = \frac{G'(x)}{G(x)} \tag{18}$$

and

$$B_x(x) = -\left[p + \frac{\partial p}{\partial x}(x - x_0)\right] \quad . \tag{19}$$

In this paper we use the time domain method that incorporates the analytic signal technique to solve for these coefficients (Langston, 2007c). Once we have $A_x(x)$, $A_y(y)$, $B_x(x)$, and $B_y(y)$, we can find the radial coefficients through:

$$A_r(r) = A_x(x)sin\theta + A_y(y)cos\theta \tag{20}$$

$$B_r(r) = B_x(x)sin\theta + B_y(y)cos\theta \quad . \tag{21}$$

The propagation azimuth angle, θ, is given by

$$\theta = tan^{-1}\frac{B_x(x)}{B_y(y)} \tag{22}$$

and the radiation pattern is represented as

$$\frac{1}{r}\Re(\theta) = A_x(x)cos\theta - A_y(y)sin\theta \quad . \tag{23}$$

There are two experiments presented in this paper that use the two-dimensional seismic-wave gradiometry formalism. The geometrical spreading and radiation pattern are products of this method, but we do not address them in these experiments. Our main goals are to investigate the accuracy of gradiometry velocity and azimuth estimates using small-scale arrays and high frequency sources, similar to experimental geometries used in exploration seismology.

Experiment Location and Instruments

Three experiments were performed in the yard of the Center for Earthquake Research and Information at The University of Memphis, Tennessee. Near the experiment site, there was a busy street, university foot-traffic, and four houses with air conditioning units causing significant ambient ground motions. We used a Geometrics Strataview seismograph with 24-channel recording to conduct all experiments. The geophones were vertical velocity sensors with a natural frequency of 28 Hz. Forty-eight geophones initially were tested in a huddle test and 24 ultimately used for the three experiments. Data were collected at a sampling interval of two milliseconds corresponding to a Nyquist frequency of 250 Hz.

A huddle test was performed in an attempt to ensure correctly functioning geophones and to pick the 24 instruments that were used in Experiments 1, 2, and 3. The geophones were clustered in a small area with about eight centimeters between geophones measured center to center. Ambient ground noise and vertical hammer sources were recorded. Obvious defective geophones were identified through review of the time series. We also attempted to calculate the relative gain specific to each geophone as an approximate way to calibrate the suite of geophones. Two groups of 12 geophones (#1-12 and #25-36) were present in the three huddle tests (Huddle Groups 1, 2, and 3). The relative gain was computed by calculating the power spectral density represented by

$$\hat{P}_i(\omega) = \hat{s}_i(\omega)\hat{s}_i^{\,*}(\omega) \tag{24}$$

where $\hat{s}_i(\omega)$ is the Fourier transform of an individual huddle test trace and $\hat{s}_i{}^*(\omega)$ is its complex conjugate. We calculated this power spectral density using Welch's method with a window of 0.4 seconds and an overlap of 50% (Welch, 1967). Next, we calculated the average in a frequency band from ω_1 to ω_2 given by

$$\overline{P_i} = \int_{\omega_1}^{\omega_2} \hat{P}_i(\omega) d\omega \tag{25}$$

where our band was 20-130 Hz due to our specified working frequency band (presented later). Then, we take an average of $\overline{P_i}$ over the N sensors present in a single huddle group:

$$P_a = \frac{1}{N} \sum_{j=1}^{N} \overline{P_i} \tag{26}$$

We then take the amplitude ratio by dividing P_a by $\overline{P_i}$:

$$r_i = \frac{P_a}{\overline{P_i}} \tag{27}$$

and, finally, the relative gain is the square root of the reciprocal of the amplitude ratio given by

$$G_i = \sqrt{1/r_i} \quad . \tag{28}$$

Huddle Groups 1, 2 and 3 contained a combination of 48 geophones. Group 1 contained geophones 1-24, Group 2 contained 25-48, and Group 3 contained 1-12 and 25-36. We compared the relative gain values from geophones 1-12 in Groups 1 and 3 and geophones 25-36 in Groups 2 and 3. For example, Geophone 10 has a relative gain value from Huddle Group 1 and a relative gain value from Huddle Group 3. Those two gain values should be the same. If they are, we could use the value to correct Geophone 10. This was not the case in our measurements; the gain values were off from each other by as much as 4.5% presumably due to geophone/ground interaction.

We determined how this error affects the results of gradiometry calculations performed with Experiment 2 and 3 data. To do this, we produced synthetic data for a five-station gradiometer cell and calculated the azimuth and slowness using wave gradiometry. The synthetic data had a cell interstation distance of 10 meters, and a wavelength of 450 meters, which results in an interstation distance that is 2.2% of the wavelength. In Experiments 2 and 3, the interstation distance was 0.5 meters and the surface-wave wavelength was 8-10 meters, resulting in an interstation distance that is 5-6.25% of the wavelength. Introduced in more detail in the Results section, the interstation distance must be less than 10% of the minimum wavelength for the wave gradiometry spatial gradient calculation to be accurate. The results for the synthetic data error calculation approximately scale to the actual array sizes and wavelengths in Experiments 2 and 3.

For the synthetic data, random gain errors with a 4.5% median were multiplied with the synthetic data, and the source was located 1 kilometer from the cell. The input azimuth was 90 degrees, and the slowness was 0.4 s/km. Figure 8 shows the result from

100,000 realizations of this Monte Carlo simulation. The mean slowness is 0.4 s/km with a standard deviation of 0.03 s/km, and the mean azimuth is 90 degrees with a 1.97-degree standard deviation. A normally distributed gain error of 4.5% applied in this way gives very good gradiometry estimates. Reasonable variations in geophone responses will not unduly affect the performance of a well-designed gradiometer.

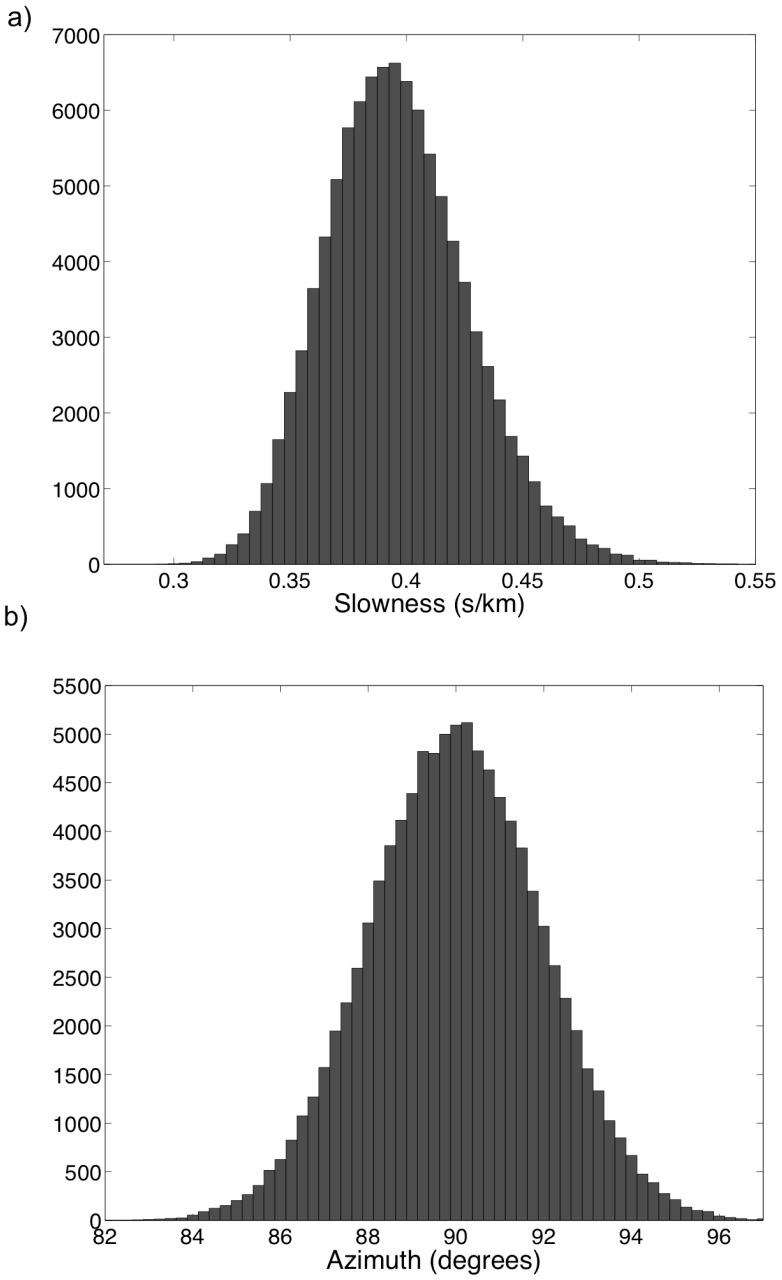

Figure 8: Monte Carlo 100,000 realizations
Monte Carlo trials of azimuth and slowness calculations using wave gradiometry for a five-station gradiometer cell with an input gain error. The source was 1 km away and the input azimuth was 90 degrees and input slowness was 0.4 s/km. There were 100,000 realizations of each five-station cell with a gain error in every waveform. The resulting mean azimuth is 90 degrees with a standard deviation of 1.97 degrees, and the resulting mean slowness is 0.4 s/km with a 0.03 s/km standard deviation.

Experimental Geometries and Motivation

The sources for Experiments 1, 2 and 3 were vertical sledgehammer hits on a metal plate (hereafter called "shots"). The locations of these shots relative to the three experiments are shown in Figure 9. Notice that there were six shot points for the P-wave refraction line, and six different shot points for Experiments 2 and 3.

Experiment 1 was done to identify the types of waves present and to provide baseline data on velocity structure for the direct and refracted P-wave arrivals as well as a dispersion curve for surface wave velocity as a function of frequency. The geophones were placed in the linear P-wave refraction line (Figure 7). Six shots were triggered with three on each side of the refraction line (Figure 9).

Experiment 2 was a compound gradiometer. This array consisted of four gradiometer cells in a linear array (Figure 7). Sources were placed at distances ranging from five to ten meter offsets. The purpose of this experiment was to investigate slowness and azimuth changes as the waves traveled across the cells and to test location abilities of the array.

Experiment 3 consisted of a "redundant" gradiometer cell consisting of clustered array elements (Figure 7). The goal with this experiment was to investigate gradiometry wave attribute precision related to the number of geophones used in the array.

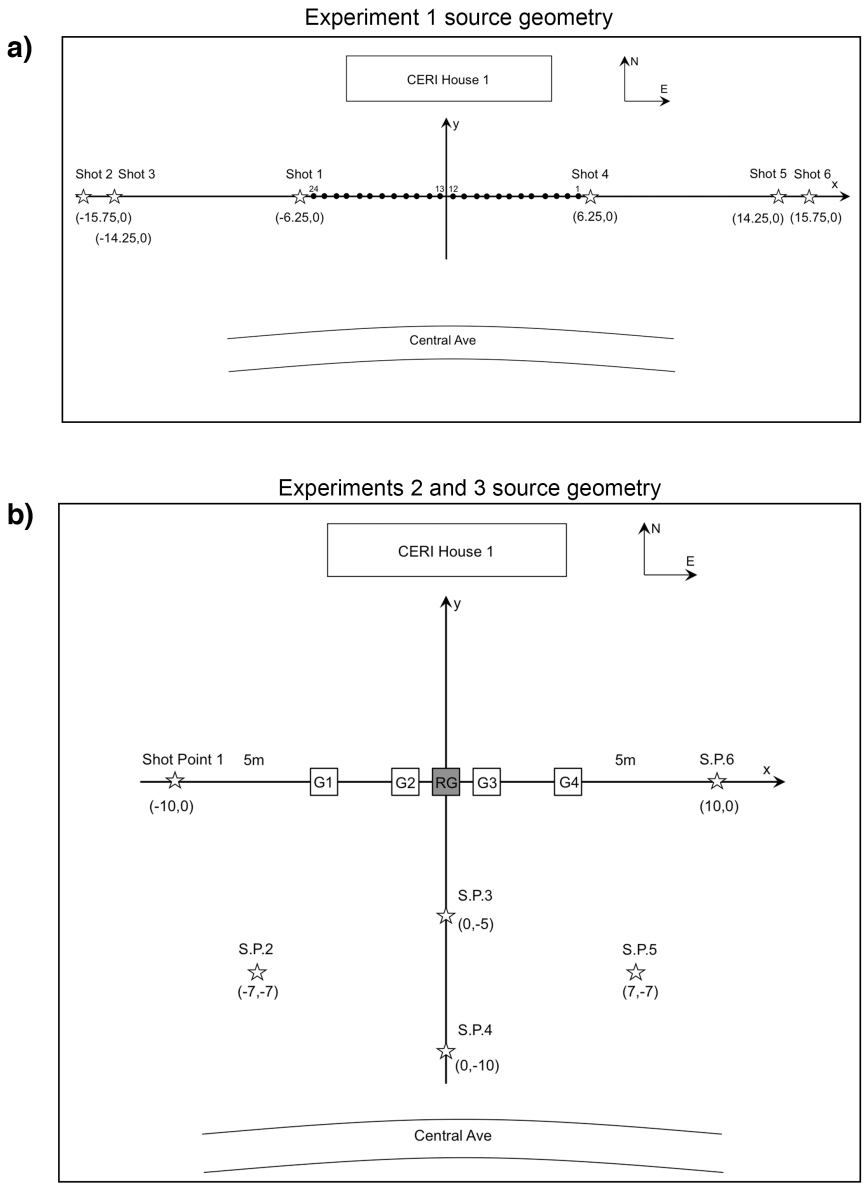

Figure 9: Source geometry
Source geometry shown to scale for Experiment 1 (a) and Experiments 2 and 3 (b). The positive *y*-axis corresponds to north and positive *x* to east. Experiment 1 source geometry consisted of six vertical hammer strikes, three on each side of the 24-station refraction line at 0.5-, 8.5- and 10-meter offsets from the ends of the line. Experiments 2 and 3 sources were vertical hammer strikes at points east, west, and south from the stations at (-10,0), (-7,-7), (0,-5), (0,-10), (7,-7), and (10,0). The boxes labeled “G1”, “G2”, “G3”, and “G4” are the four-gradiometer cells of Experiment 2, and the grey box labeled “RG” is the Experiment 3 placement.

Results

Experiment 1

The P-wave refraction line from Experiment 1 provided the horizontal velocities of the direct and refracted P wave as well as dispersion for the surface waves. Figure 10 shows the waveforms from the east-side shots. In this figure, some waveforms overlap because some offsets share common shot-station distances. The direct and refracted P-wave arrivals have velocities of 165 m/s and 675 m/s, respectively. The zoomed-in inset of the P waves shows the change from direct to refracted wave around 0.005 km and a small increase in refracted wave velocity around 0.013 km.

The dispersion curve is shown in Figure 11 for all shots. One-dimensional frequency-slowness spectra were produced for all shots separately and then averaged together. Dominant velocities are 3-5 s/km (333-200 m/s) in the frequency band of 20-40 Hz. These results will be used to verify the slowness outcomes from Experiments 2 and 3.

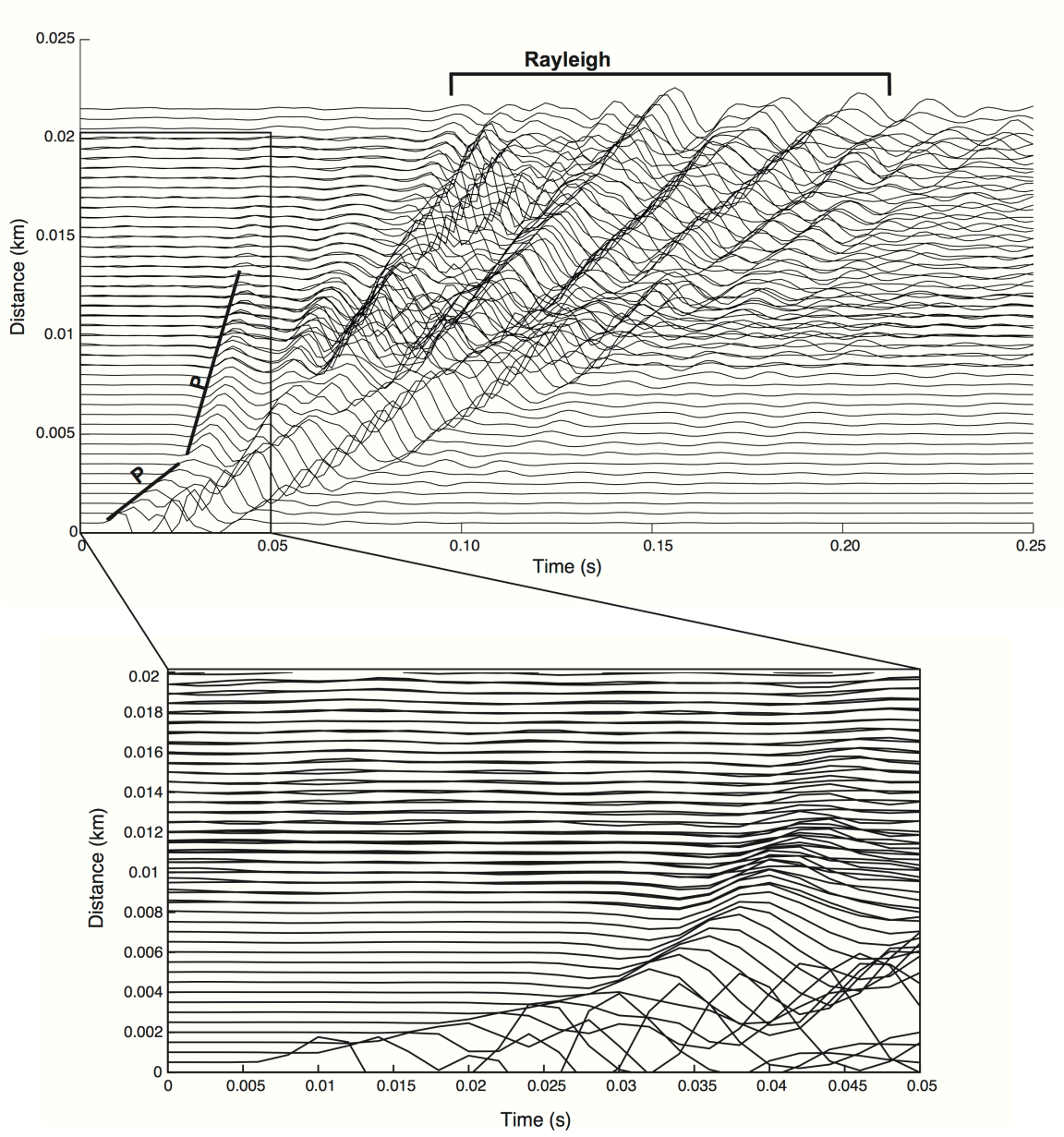

Figure 10: Experiment 1 waveforms
Experiment 1 waveforms from the eastern shots: shots #4, 5, and 6 at 0.5, 8.5 and 10-meter offsets from the eastern-most geophone. The phases labeled are the direct P wave (to an offset of 3 meters), the refracted P wave (greater than 3-meter offset), and dispersed Rayleigh waves. The plot at the bottom shows an expanded section of the P wave arrivals with an amplitude increase to better see the change from direct to refracted wave. Noticeable on this plot, too, is a jump in the refracted wave velocity around an offset of 13 meters.

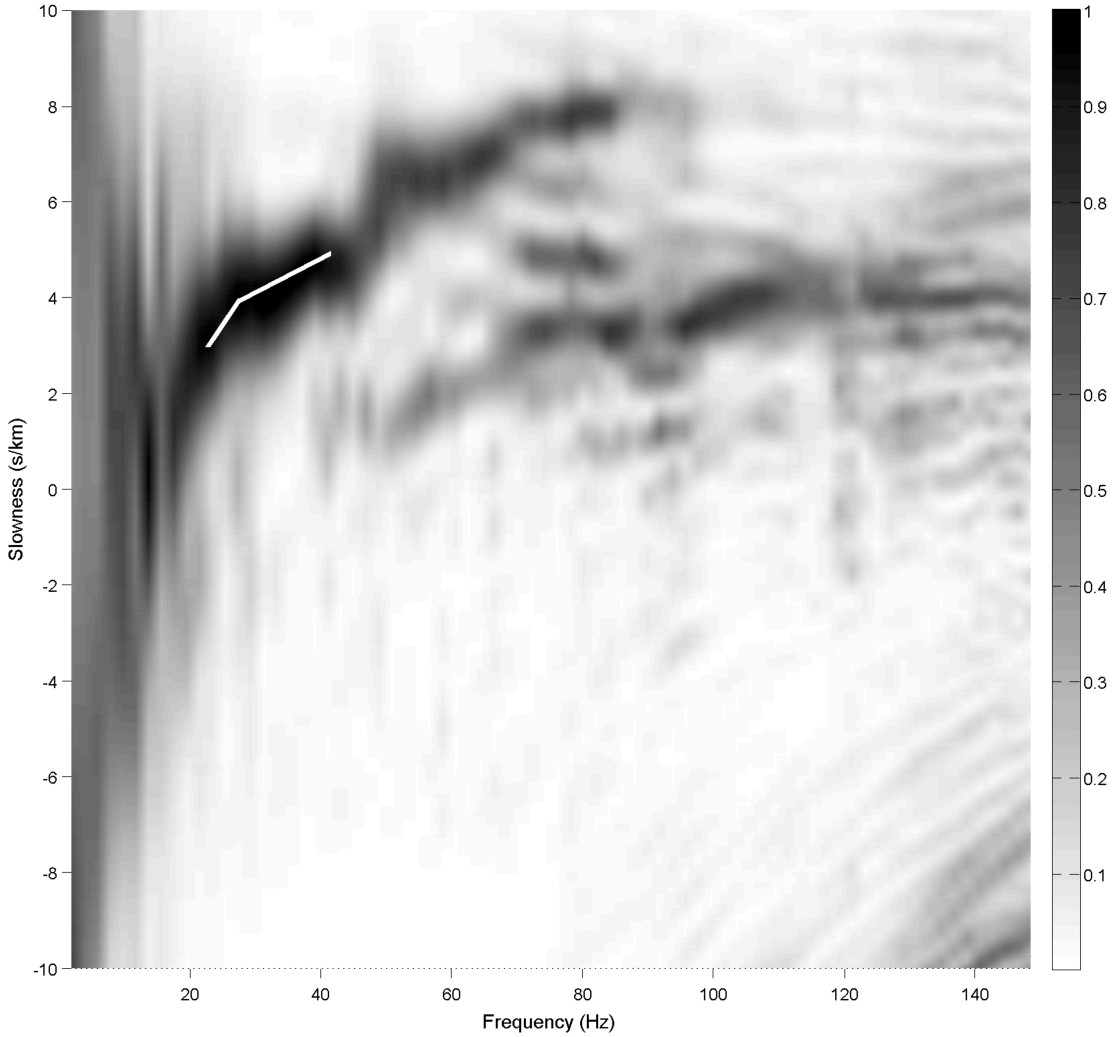

Figure 11: One-dimensional frequency slowness spectra
One-dimensional frequency slowness spectra from the Experiment 1 refraction data, The resulting plot allowed us to pick the frequency range of the fundamental mode surface wave and provided the target surface wave frequency band for Experiments 2 and 3. The data were normalized for geometrical spreading, and the fundamental mode is highlighted with a white line.

Experiment 2

The Experiment 2 objective was to examine the consistency of wave azimuth estimates from various source locations assuming ideal wave propagation in a vertically inhomogeneous structure. The data are filtered in a frequency range appropriate for the station spacing of the gradiometers. In order to compute spatial gradients with an error of less than 10% using a first-order Taylor's expansion, we must employ a relationship that restricts the station interval based on the horizontal wavelength, given by

$$0.123\lambda_{min} \geq \Delta h \geq 0.012\lambda_{max} \tag{29}$$

where Δh is the station interval, λ_{min} is the minimum resolvable horizontal wavelength, and λ_{max} is the maximum resolvable horizontal wavelength (Langston, 2007b). Our gradiometer cells have a Δh of 0.5 meters, and with a P-wave velocity of 675 m/s, the allowable frequency range is approximately 16-166 Hz. We filtered our data inside this workable frequency range from 20-115 Hz for the P-wave arrivals. The surface waves are resolvable in the range of 8-50 Hz using equation 29. Based on the dispersion curve results from the Experiment 1, we filtered the data in the 20-40 Hz range. The data are shown in Figure 12 for Shot Points 1 and 4. Because Shot Point 1 was in the same axis as the linear array, we can see the waveforms separated in space and the arrivals separated in time. Shot Point 4 was located in the middle but 10 meters from the array, so the stations mirroring each other over the *y*-axis had equivalent shot-station distances, and these waveforms are not easily discernable like those from Shot Point 1.

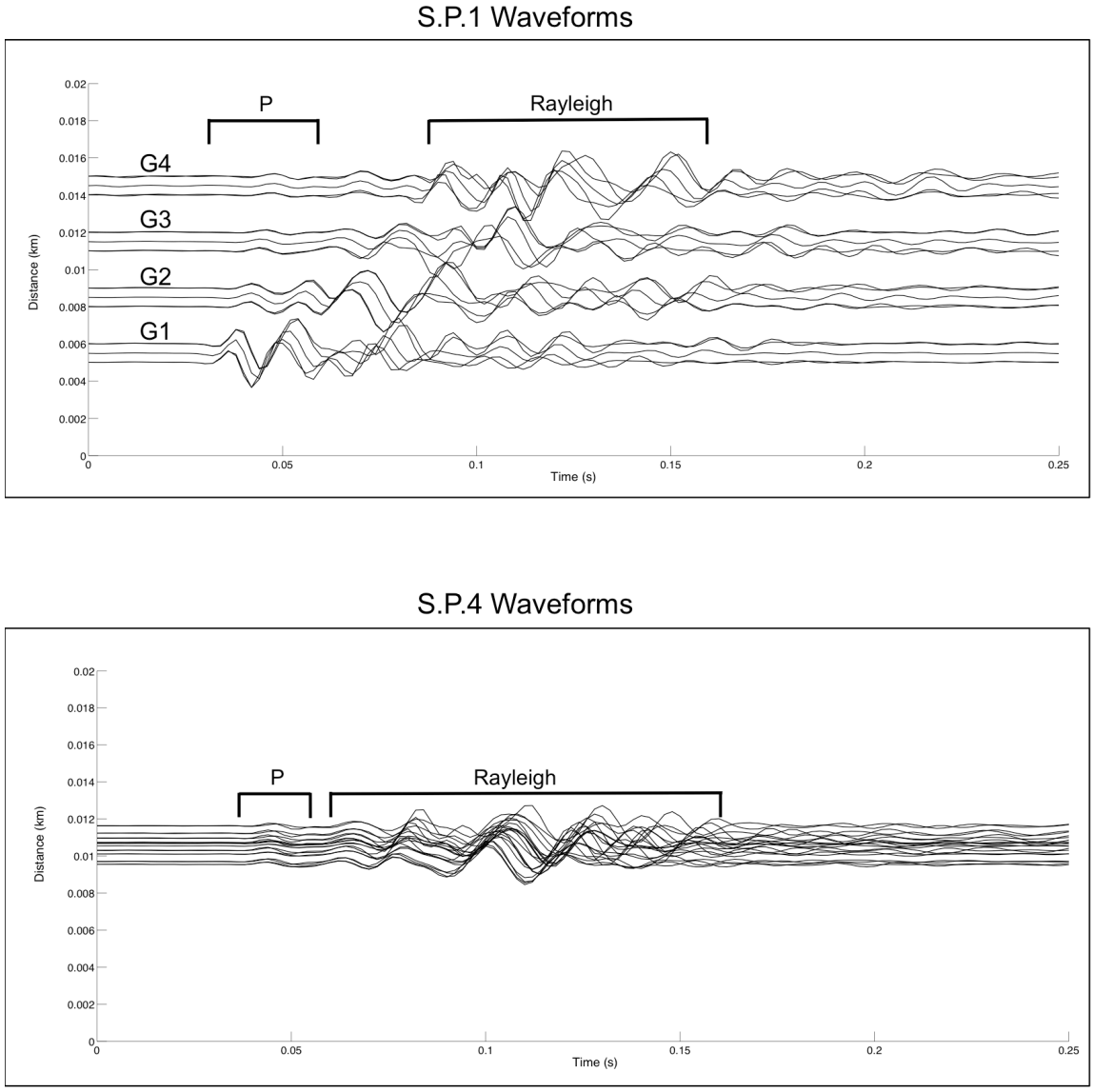

Figure 12: Experiment 2 data
Experiment 2 data from sources at Shot Points 1 (S.P. 1) and 4 (S.P. 4). The *y*-axis measures distance from the source, and the scales are the same for both plots. The labels "G1", "G2", "G3", and "G4" represent the waveforms at each of the gradiometer cells. Data were filtered 20 to 115 Hz, and the phases labeled represent P and surface waves.

A way to visualize the slowness and propagation azimuth of the waves at these four cells is shown in Figure 13. Slowness-azimuth vectors for each data point are plotted on top of the center-station seismogram. There is a plot for each of the gradiometer cells for waves traveling from Shot Point 4. The cutoff for plotting vectors was slowness values of 0 and greater than 10 s/km. The plots show that the slowness for the first arrival is less than that for the second arrival (interpreted as P and surface wave arrivals, respectively). The azimuth estimates in the time range of 0.07 to 0.13 seconds are consistent with the calculated azimuth pictured in the upper right hand corner.

In the "stable" range of 0.07 to 0.13 seconds, we randomly picked an azimuth for each cell and calculated where those azimuths intersect in space. This Monte Carlo process was done 1,000 times (Figure 14). We see that the actual source position (black circle) and the maximum of the azimuth intersections (high on the density plot) are not in the same position; they are 7.25 meters apart. The density plot does not give us our exact answer, but the intersection of the average of cells 2 and 3 give an answer very close to the actual source: the white dot closest to the black dot. The location error in this case is only 1.38 meters. In order to have a better chance of finding the source position, we would need to have gradiometer cells with some variation in the *y* direction and, ideally, cells all around the source. There is no reason that all of the cells should agree on a single source point, either. The subsurface structure in which the experiment was done is unknown and could have focusing paths or strong reflectors that cause the waves to go in other directions, which would cause the azimuth estimates to not point back to the original source. The individual cell azimuths are stand-alone and should be interpreted as such.

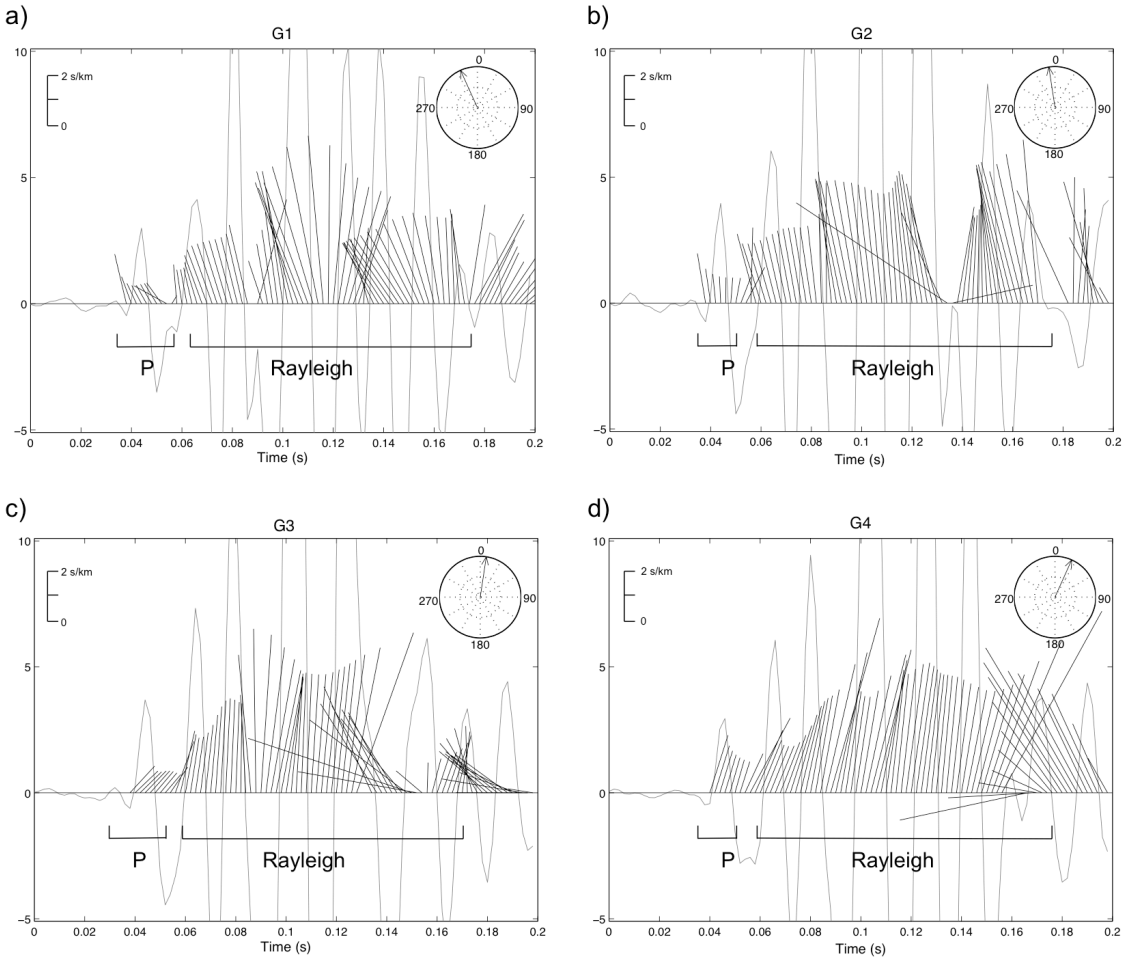

Figure 13: Experiment 2 feather plots
Experiment 2 "feather plots" showing slowness-azimuth vectors for each point plotted on top of the center station waveforms for each of the gradiometer cells. The black straight lines are the vectors, and the grey waveform is that from the center station, the upper right-hand compass is the expected vector direction based on source-station azimuth, and the upper left-hand slowness scale corresponds to vector length. P and Rayleigh waves are labeled on each plot, and the data were filtered 20 to 115 Hz.

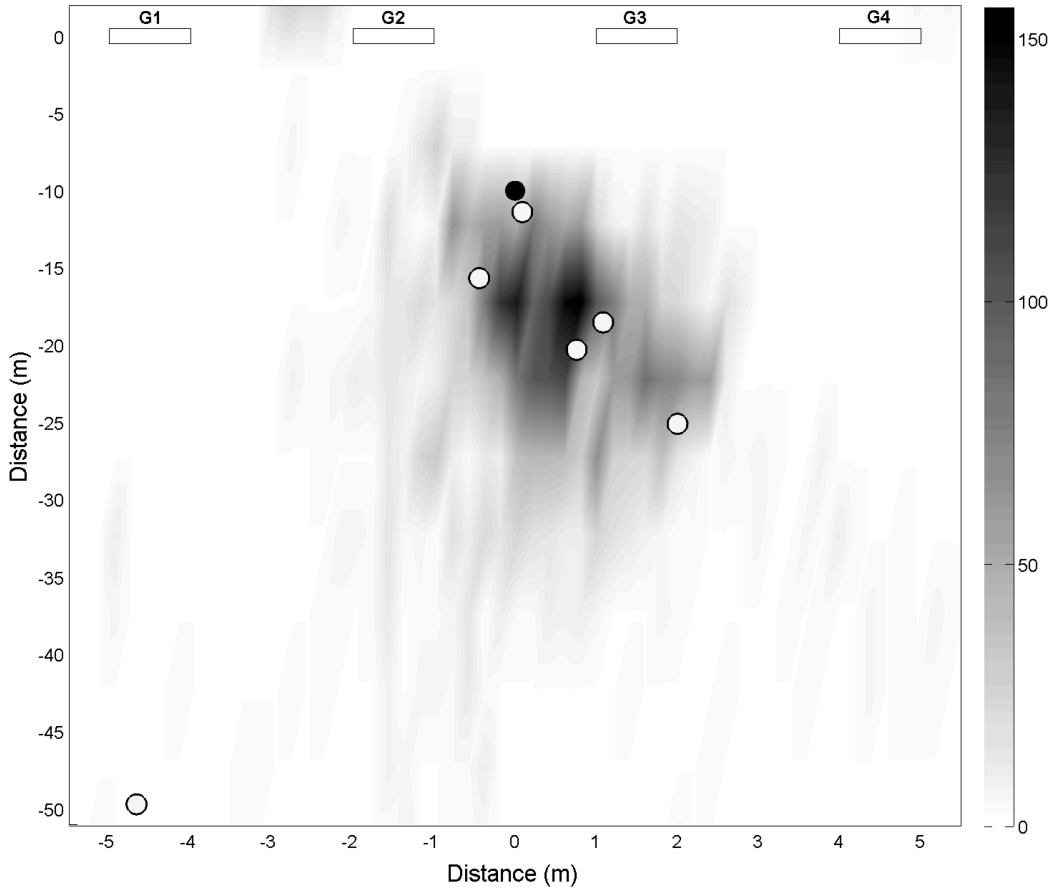

Figure 14: Experiment 2 location density plot
Density plot of Experiment 2 azimuth intersections chosen randomly for each cell from 0.07 to 0.13 seconds with 1,000 realizations. The data were binned with 0.2-meter increments in *x* and 5-meter increments in *y*, and the color bar on the right shows how many intersections fall into each bins. Cells 1 through 4 are shown in their position relative to the density plot, and the filled in black circle is the actual position of the source. The white filled in circles are the intersections of the average azimuth of each cell in the 0.07 to 0.13 second band. The plot is shown with a 5-to-1 horizontal exaggeration.

Experiment 3

Experiment 3 involved seven gradiometer configurations to investigate the scatter in the gradiometry parameters as the number of stations increased. Figure 15 shows the station set up for each of our geometries. Because of the frequency limits due to spacing as discussed in Experiment 2 Results section, a station spacing of 0.35 to 0.6 meters corresponds to a frequency range of 22-138 Hz for P-waves. We chose to filter the data in that range to 25-130 Hz. For surface-wave arrivals, the resolvable frequency range is 11-41 Hz, and the data were filtered 20-40 Hz according to the dispersion curve results from Experiment 1. Figure 16 illustrates the slowness and azimuth results for the peak of the first P-wave arrival and first surface-wave arrival from Shot Point 1.

The results from Experiment 3 tell a clear story: when we use more center stations in the gradiometer cell, our slowness and azimuth results become more precise. The individual outside configurations shown in Figure 15 do not impact the precision measurements. Each configuration has a range of values for the P-wave slowness with one center station. As more outside stations are included (going from 4 with RBCCA to 12 with RHALL), the range of slowness values does not decrease as expected. The range in P-wave slowness values only decreases as more center stations are added and averaged together (as *x* increases in Figure 16 plots a-d). In Figure 16a, the original P-wave slowness spread for RHALL with one center station is 0.255 s/km and when two center stations are used, the precision increases by 67.6% to 0.082 s/km. This trend is also seen in the second plot, 106, where the original RHALL P-wave azimuth spread is 0.977 degrees and the precision increases by 61.5% to 0.376 degrees. In the third plot, 16c, the surface-wave spread with one center station in RHALL is 0.233 s/km and the range

decreases by 44.5% down to 0.130 s/km. The last plot, 16d, shows the same trend: the surface-wave azimuth range is 0.685 degrees with just one center station, and the precision increases by 79.1% down to 0.143 degrees.

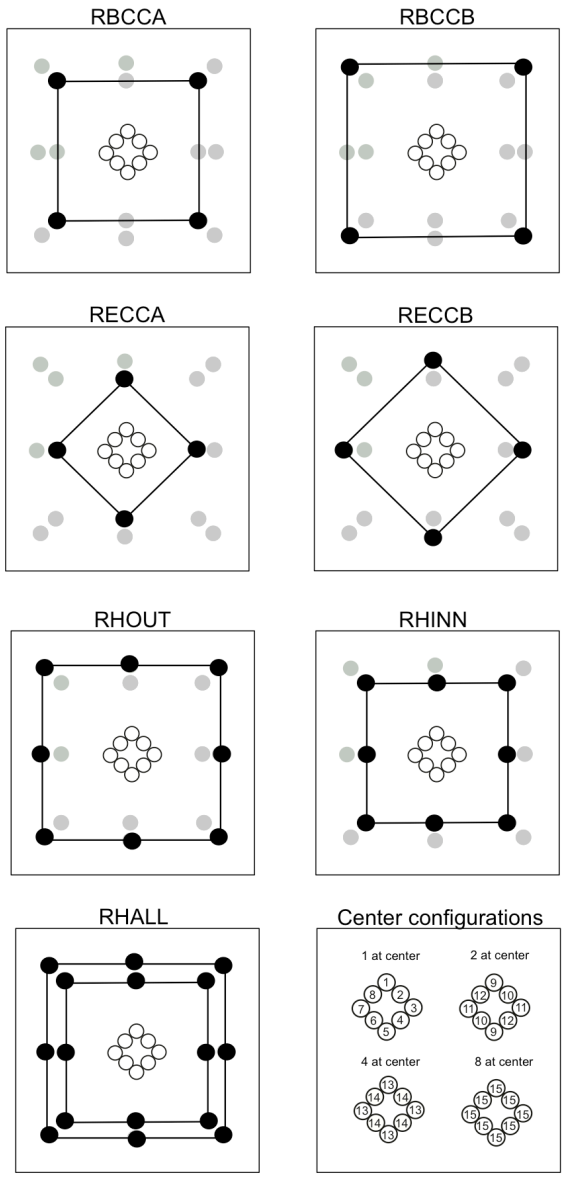

Figure 15: Experiment 3 gradiometer cell geometries
Experiment 3 gradiometer cell geometries. RBCCA, RBCCB, RECCA, and RECCB contain four of the outside stations, RHOUT and RHINN contain eight of the outside stations, and RHALL contains all sixteen outside stations. As shown in the bottom-right box, all of these station configurations used a combination of the eight inside stations: each one on its own, four combinations of two averaged stations, two combinations of four averaged stations, and all eight stations averaged together. These configurations can help us determine how scatter in wave parameters varies with the number and configuration of stations. Geophone calibration can cause problems in slowness and azimuth result accuracy, so having many center stations to average together can help rid the experiment of calibration uncertainties.

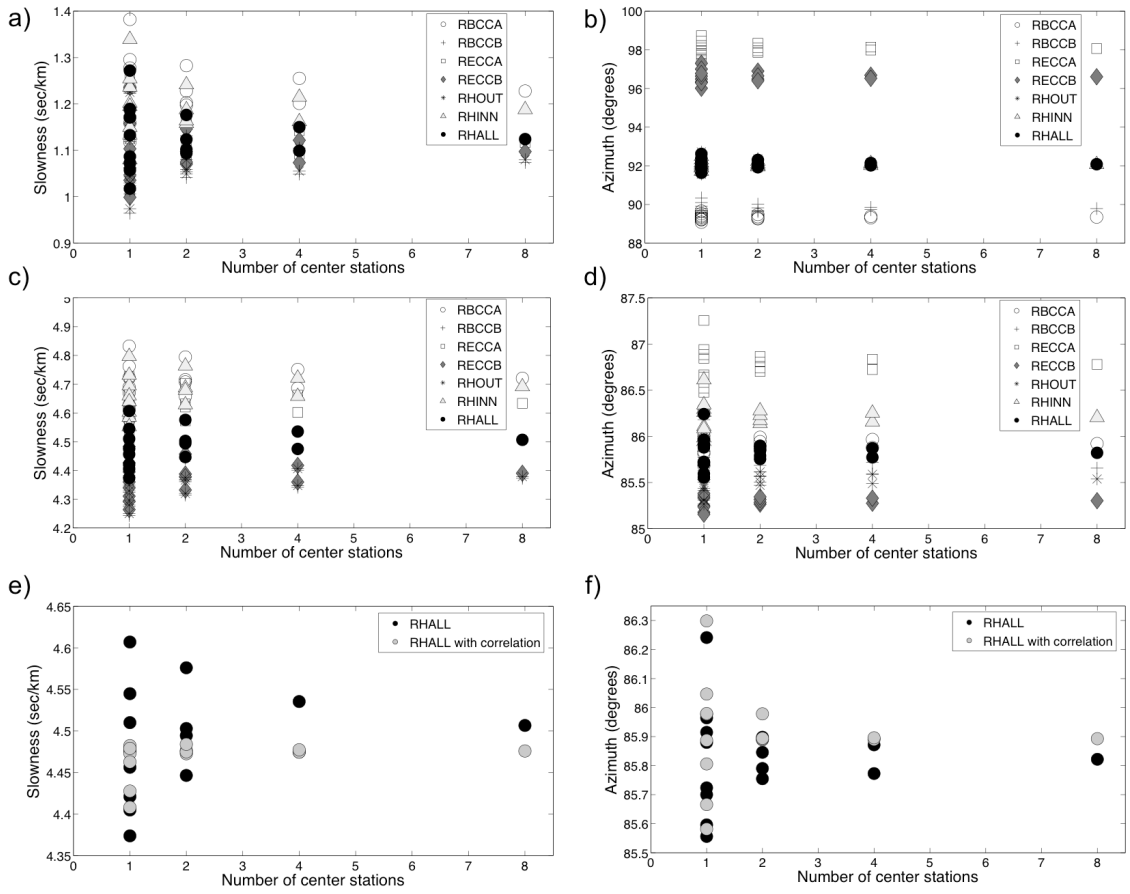

Figure 16: Experiment 3 scatter plots
Experiment 3 scatter plots showing number of center stations involved in solving for the spatial gradient versus P-wave slowness (a), P-wave azimuth (b), surface-wave slowness (c), and surface-wave azimuth (d). As the number of center stations increased (increasing *x*), the range of slowness and azimuth values decreased. Plots e and f show scatter plots of original RHALL surface wave slowness estimates (e) and azimuth estimates (f) as black dots, and the same data processed using the center-station correlation method (grey dots).

This result can be explained using the matrix representation of the spatial gradient equation. The spatial gradient is a result of a simple inversion problem involving the displacement measurements at the locations of stations in the cell (Liang and Langston, 2009):

$$\begin{bmatrix} u_1 - u_0 \\ u_2 - u_0 \\ \vdots \\ u_N - u_0 \end{bmatrix} = \begin{bmatrix} \delta x_1 & \delta y_1 \\ \delta x_2 & \delta y_2 \\ \vdots & \vdots \\ \delta x_N & \delta y_N \end{bmatrix} \begin{bmatrix} \partial u/\partial x \\ \partial u/\partial y \end{bmatrix} \tag{30}$$

where u_i is the displacement measurement at each station, u_0 is the displacement at the center station, δx_i and δy_i are the *x* and *y* distances from each station to the center station, and $\partial u/\partial x$ and $\partial u/\partial y$ are the spatial gradients in *x* and *y*, respectively. The range in measurements with one center station in Figure 16 is due to an amplitude error in the center station displacement measurements. With the amplitude error, the u_0 in equation 30 is actually $(1 + a)u_0$ where *a* is some amplitude error. Since this variable is present in every row of the left-hand side of equation 30, the final spatial gradient results inherit the error, which is reflected in the resulting slowness and azimuth estimates. If we, instead, average together multiple center stations and use that average as the center station displacement measurement, the variable becomes $\frac{1}{N}(u_{0_1} + u_{0_2} + \cdots + u_{0_N})$. Using this averaging, the amplitude error in one of the center stations is less affective; this is visible in Figure 16 plots a-d as more center stations are averaged (as *x* increases). An amplitude error in any of the outside stations contributes less error to the overall

answer because the displacement measurement at each outside station is only present in one row of the left-hand side of equation 30.

Since it is not regular practice to group eight geophones at a center point in hopes of averaging their displacement measurements to avoid amplitude errors, we propose using a center-station correlation method. This method correlates each outside station displacement with the center station displacement to find the proper time shift and then averages the time-shifted waveforms. Using this new waveform average as the center station displacement and keeping the outside station displacements in their original form reduces the effects of center-station amplitude errors as shown in Figure 16 plots e and f. Plot 16e shows how the center-station correlation improves the RHALL surface-wave slowness measurements for one and two center stations. The range with one center station for the original RHALL slowness is 0.233 s/km while the range for the center-station correlated RHALL is 0.074 s/km. The center-station correlated RHALL surface-wave azimuth range with one center station did not improve on the original RHALL azimuth range; the original was less than one degree, which is quite precise.

Discussion

Both Experiments 2 and 3 velocity results agree with the results found from the Experiment 1 velocities for P- and surface-wave arrivals. The Experiment 1 velocity results were 675 m/s for the refracted P-wave arrival and 200-333 m/s for surface wave arrivals. For Experiment 2, the average P-wave velocity for distances of 5.2 to 14.5 meters was 550.7 m/s with a standard deviation of 224.5 m/s and the average surface-wave velocity was 245.5 m/s with a standard deviation of 45 m/s. The standard deviation in Experiment 2 P-wave velocity values is possibly due to the wide range in shot to

station distance. The first arrival picks at the distance ranges between 5.2 to 14.5 meters could be sampling different phases and taking an average of all of the velocity picks would be erroneous. In Experiment 3, the average P-wave velocity for RHALL with eight center stations at a shot distance of ten meters was 1,034.7 m/s with a standard deviation of 86.5 m/s over a 0.008 second band, and the surface-wave velocity was 222.4 m/s with a 15.9 m/s standard deviation over a 0.048 second band. The P-wave slowness is larger than we would expect, but the surface-wave slowness is in the correct range.

In both Experiments 2 and 3, the surface-wave velocity agrees very well with the Experiment 1 dispersion curve velocity results compared to how the P-wave velocity values match up. This correlation agrees with a result from Liang and Langston (2009) where they derive a relation between truncation errors present in taking into account only the first order of a Taylor's series when solving for the spatial gradient. Liang and Langston (2009) show that the truncation error is proportional to frequency and station spacing and inversely proportional to phase velocity. We can interpret the relation as the error being proportional to the station spacing and inversely proportional to the wavelength. The surface waves targeted in Experiments 2 and 3 are longer wavelength waves than the P waves, so we would expect higher errors in P-wave slowness and azimuth results.

The results from the huddle test show that off-the-shelf geophones have inherent error and that with a normally distributed gain error, the synthetic gradiometry results using a Monte Carlo routine produced a peak at the input slowness and azimuth. The slowness and azimuth results on either side of the peak can also help explain some of the deviation of Experiments 2 and 3 from the Experiment 1 velocities and expected azimuth.

The main result from Experiment 3 agrees with results published from Suryanto et al. (2006). In their experiment, they compared Sagnac ring laser rotation results against array-derived rotations for three stations and again with nine stations. They found that as more stations were included in the rotation calculation, the results had better agreement with ring laser results indicating that random errors or systematic differences in parts of the array may cancel out with more stations used. We observed a slight variation on this conclusion: as more center stations were included in the gradiometer cells, the measurements became more precise because random amplitude errors were being averaged out, but there was no improvement on measurements obtained using more outside stations in the gradiometer cell.

Conclusion

Horizontal slowness and propagation azimuth from two, two-dimensional dense seismic-arrays agreed with results from a linear refraction line and expected direction. Slowness-azimuth vectors from Experiment 2 clarify wavefield visualization, and the location abilities prove possible and increasingly more accurate with an increase in gradiometric cells around the source. Scatter plots from Experiment 3 clearly illustrated the decrease in slowness and azimuth range with the increase in center stations. A drawback of this technique, as shown in the huddle test, is that the results are sensitive to uncalibrated instruments.

The experiments have shown that seismic-wave gradiometry is reliable with off-the-shelf geophones and it produces good results for dense, small-scale datasets. Geometrical spreading and radiation pattern changes are two results produced with two-dimensional arrays that can tell more about the wavefield than with only horizontal

slowness and azimuth. The next step is to expand the number of gradiometric cells to a larger region in order to produce wave attribute maps, which can be interpreted to tell us how the waves are traveling and possible subsurface reasons for scattering.

Small, dense arrays analyzed as we have done here can be useful in exploration seismology. Maps of slowness, azimuth, geometrical spreading, and radiation pattern can be interpreted in conjunction to give more information than was previously common about the wavefield. The fact that gradiometry utilizes station spacing that is less than common stacking methods means that these arrays are easier to deploy and less invasive.

References

Hinich, M. J., 1981, Frequency-wavenumber array processing: The Journal of the Acoustical Society of America, **69**, 732-737.

Langston, C. A., 2007a, Spatial gradient analysis for linear seismic arrays: Bulletin of the Seismological Society of America, **97**, no. 1B, 265-280.

Langston, C. A., 2007b, Wave gradiometry in two dimensions: Bulletin of the Seismological Society of America, **97**, no. 2, 401-416.

Langston, C. A., 2007c, Wave gradiometry in the time domain: Bulletin of the Seismological Society of America, **97**, no. 3, 926-933.

Liang, C., and C. A. Langston, Wave gradiometry for USArray: Rayleigh waves: Journal of Geophysical Research, **114**, doi:10.1029/2008JB005918.

Suryanto, W., H. Igel, J. Wassermann, A. Cochard, B. Schuberth, D. Vollmer, F. Scherbaum, U. Schreiber, and A. Velikoseltsev, 2006, First comparison of array-derived rotational ground motions with direct ring laser measurements: Bulletin of the Seismological Society of America, **96**, 2059-2071.

Welch, P. D., 1967, The use of fast Fourier transform for the estimation of power spectra: A method based on time averaging over short, modified periodograms: IEEE Transactions on Audio Electroacoustics, **AU-15**, no. 2, 70-73.

CHAPTER 4

SEISMIC-WAVE GRADIOMETRY WITH A DENSE, 2D ARRAY

Introduction

Langston (2007 a-c) published a theory of using wave gradients, called seismic-wave gradiometry (WG), to analyze wave attributes from seismic recordings. A number of previous studies have demonstrated the range of applications of this theory. Langston et al. (2009) analyzed data from borehole-explosions at a collection of 11 strong motion stations. Because this array was rather small, it could serve as a "gradiometer" where wave spatial gradients could be estimated from the seismic recordings. They found that phase slowness and propagation azimuth were key in determining the scattering properties of the waves in the particular river valley where the experiment took place. Using the USArray stations in the western part of the United States, Liang and Langston (2009) applied WG to Rayleigh waves recorded from nine earthquakes with varying azimuths. They created individual gradiometers over the approximately 400 USArray stations to show how wave parameters changed with distance from the earthquake. They were able to generate wave characteristic maps and showed that the phase velocity maps agreed with global averages of Rayleigh waves.

Array processing techniques treat each element in an array as a point measurement but the accumulated effects of wave scattering over the whole raypath are often reflected in the results (Liang and Langston, 2009). WG is used to generate phase velocity, directionality, and amplitude variation (geometrical spreading and radiation pattern) maps in order to examine the effects of a local or regional media over an area in an effort to more precisely measure the variability.

We will use WG to analyze a unique dataset acquired in eastern Ohio for a dense array situated above a heavily coal mined area. The array consists of 376 stations spaced ~34 meters apart that recorded buried 1kg dynamite shots at distances of 314 meters to 2700 meters. This allows the opportunity to analyze a high-frequency, exploration seismology dataset for shots from varying azimuths to investigate the stability of WG estimates of wave attributes and to infer information about the wavefield. In addition to the WG processing methods introduced in the Langston papers (2007a-c), we introduce an amplitude correction method to minimize the effect of geophone amplitude statics. The original intent of this study was to apply WG to dense array data to obtain wave attribute maps that could directly, and empirically, illuminate mined out areas under the array. However, results will show that surface and body wave fields are highly heterogeneous across the array and it is difficult to ascribe wave attributes to particular spatial positions, unlike results from simple 3D synthetic models.

Methods

Data

The deployment, collection, and processing of data from the dense array in Belmont County, Ohio was an effort between Global Geophysical Services (deployment and collection) and The Center for Earthquake Research and Information at The University of Memphis (processing). Global Geophysical Services performed a joint 3D seismic shoot with Hess Corporation in eastern Ohio and generously augmented their array with our proposed dense, smaller array. The sources were 1-kg dynamite shots at 6.1-meter depth, and they were spaced every 67 meters on lines spaced 402 meters apart. We chose 29 shots with good signal-to-noise ratio waveforms with varying azimuths around the array. The locations of the shots and the 376 stations are shown in Figure 17.

The 29 shot locations are shown as gray circles, and the 376 station locations are shown as black triangles; the area of the box is 2.88 by 3.8 km. Sources were 1-kg dynamite shots buried 6.1 meters. Shots #48703, #47918, and #48756 are labeled because we analyze these shots specifically in the Results section. The station array is approximately 360 by 650 meters. The closest shot-to-station distance is 314.4 meters and the farthest is 2687.9 meters. North points up in the figure.

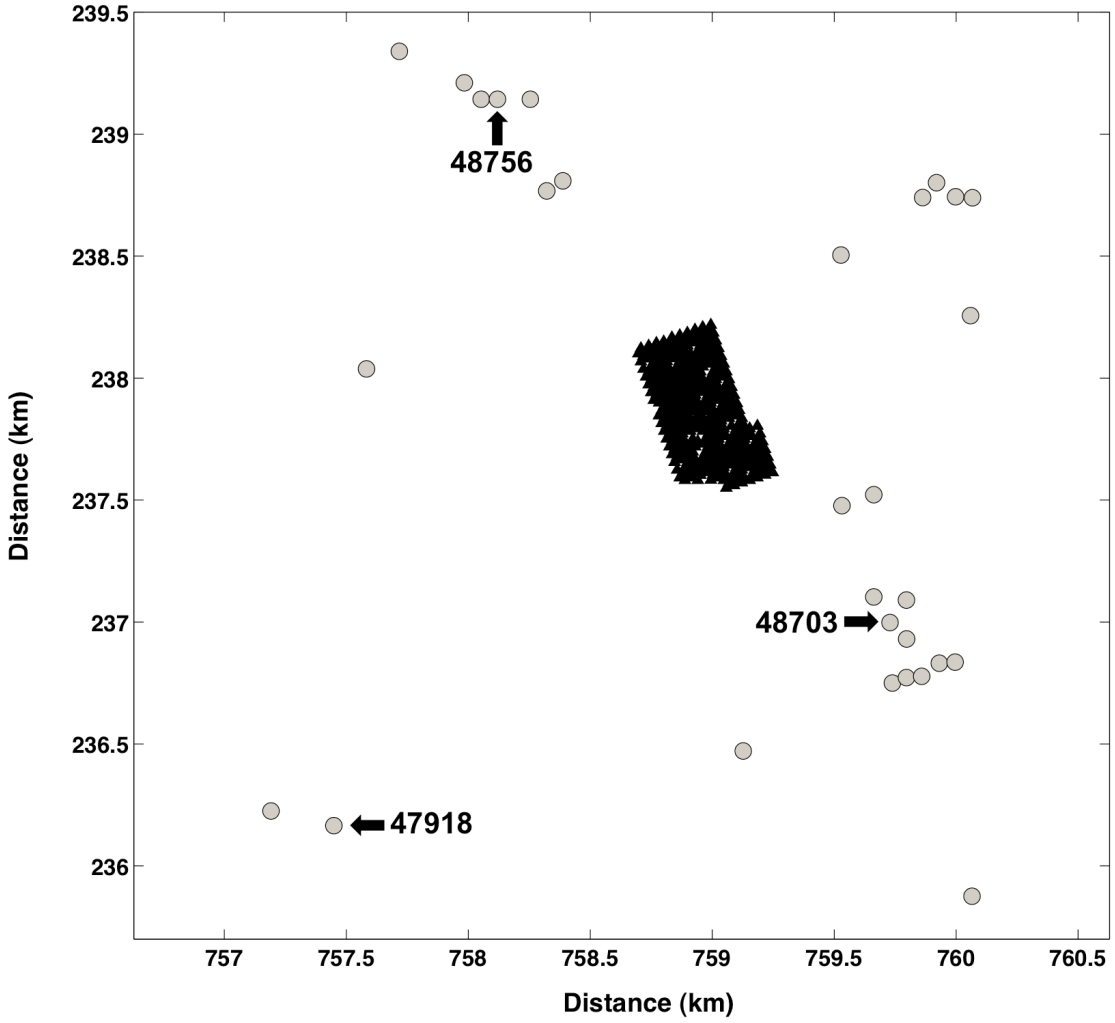

Figure 17: Source and station geometry
The 29 shot locations are shown as gray circles, and the 376 station locations are shown as black triangles; the area of the box is 2.88 by 3.8 km. Sources were 1-kg dynamite shots buried 6.1 meters. Shots #48703, #47918, and #48756 are labeled because we analyze these shots specifically in the Results section. The station array is approximately 360 by 650 meters. The closest shot-to-station distance is 314.4 meters and the farthest is 2687.9 meters. North points up in the figure.

The stations in our dense array were 33.6 meters apart on 23 lines spaced 16.8 meters apart. The station lines had staggered starting points, so two stations on a line next to each other were 33.6 meters apart. An abbreviated version of the array is shown in Figure 18 to illustrate this concept. The dense array covered an area of approximately 360 by 650 meters. The shots we received were in a 3962-meter radius of the array from August 25 to September 7, 2013.

The bedrock geology of the eastern Belmont County region of Ohio consists of Permian-Pennsylvanian-age sedimentary rocks of mainly shale, sandstone, siltstone, mudstone, and coal and the region is also heavily coal mined (Ohio Division of Geological Survey, 2006). The array was placed above unmined strata as well as two mines on the northern and southern end of the array: Florence (BT 187) abandoned in 1961 and Gaylord No. 1 (BT 203) abandoned in 1940. Both of these mines were room and pillar mines with an average depth of 122 meters. These mines are most likely filled with water (Daniels, 1988) and should represent strong velocity heterogeneity in the survey area.

2D wave gradiometry

Seismic-wave gradiometry is an array processing technique that was first described in a series of papers (Langston 2007a, 2007b, 2007c) aimed at characterizing the wavefield by exploiting the difference in wave amplitude at stations in a small array, or cell. The method relies on the computation of an accurate spatial gradient between a reference station and a minimum of five other stations in the cell. We use a second order Taylor's series approximation of the spatial gradient of the form:

$$du_i = u_i - u_0 = \delta x_i \frac{\partial u}{\partial x}\Big|_{S_0} + \delta y_i \frac{\partial u}{\partial y}\Big|_{S_0} + \delta x_i^2 \frac{\partial u^2}{2\partial^2 x}\Big|_{S_0} + \delta y_i^2 \frac{\partial u^2}{2\partial^2 y}\Big|_{S_0} + \delta x \delta y \frac{\partial u^2}{\partial x \partial y}\Big|_{S_0} \quad (31)$$

where $u_i, i = 1{:}N$ stations, is the wave function at the receivers, u_0 is the wave function at the reference station, $\delta x_i = x_i - x_0$, and $\delta y_i = y_i - y_0$. Equation 1 can be written in matrix form:

$$\begin{bmatrix} u_1 - u_0 \\ u_2 - u_0 \\ \vdots \\ u_N - u_0 \end{bmatrix} = \begin{bmatrix} \partial x_1 & \partial y_1 & \partial x_1^2 & \partial y_1^2 & \partial x_1 \partial y_1 \\ \partial x_2 & \partial y_2 & \partial x_2^2 & \partial y_2^2 & \partial x_2 \partial y_2 \\ \vdots & \vdots & \vdots & \vdots & \vdots \\ \partial x_N & \partial y_N & \partial x_N^2 & \partial y_N^2 & \partial x_N \partial y_N \end{bmatrix} \begin{bmatrix} \partial u / \partial x \\ \partial u / \partial y \\ \partial u^2 / 2\partial^2 x \\ \partial u^2 / 2\partial^2 y \\ \partial u^2 / \partial x \partial y \end{bmatrix} \quad (32)$$

and it can be solved using least squares inversion. A minimum of six total stations, including the reference station, are required in this experiment to produce a five-row vector on the left-hand side of Equation 2 and make the system invertible.

Following Langston (2007b), the wave function can be written in terms of geometrical spreading ($G(x, y)$), phase variation ($f(t, x, y)$), and slowness (p_x and p_y) as:

$$u(t, x, y) = G(x, y) f(t - p_x(x - x_0) - p_y(y - y_0)) \quad (33)$$

Differentiating Equation 3 with respect to *x* and *y* gives

$$\frac{\partial u(t,x,y)}{\partial x} = A_x(x)u(t,x,y) + B_x(x)\frac{\partial u(t,x,y)}{\partial t} \tag{34}$$

and

$$\frac{\partial u(t,x,y)}{\partial y} = A_y(y)u(t,x,y) + B_y(y)\frac{\partial u(t,x,y)}{\partial t} \tag{35}$$

where

$$A_x = \frac{1}{G(x,y)}\frac{\partial G(x,y)}{\partial x} \quad , \tag{36}$$

$$A_y = \frac{1}{G(x,y)}\frac{\partial G(x,y)}{\partial y} \quad , \tag{37}$$

$$B_x(x) = -\left[p_x(x) + \frac{\partial p_x}{\partial x}(x - x_0)\right] \quad , \tag{38}$$

and

$$B_y(y) = -\left[p_y(y) + \frac{\partial p_y}{\partial y}(y - y_0)\right] \quad . \tag{39}$$

To solve Equations 4 and 5 for A_x, A_y, B_x, and B_y, we use a time domain method based on the analytic signal (Langston, 2007c). The Cartesian coefficients are converted into radial coefficients:

$$A_r(r) = A_x(x)sin\theta + A_y(y)cos\theta \tag{40}$$

and

$$B_r(r) = B_x(x)sin\theta + B_y(y)cos\theta \tag{41}$$

where

$$\theta = tan^{-1}\frac{B_x(x)}{B_y(y)} \quad . \tag{42}$$

$B_r(r)$ represents the radial slowness, θ represents the propagation angle, and $A_r(r)$ represents the change in geometrical spreading. These parameters are calculated for each time point and are specific to the reference station position.

Amplitude correction

To avoid amplitude errors due to geophone calibration and siting effects, we performed an amplitude correction using nearby subsets of the array data. First, we detrended the data and then removed any station whose waveforms were larger than four times the average waveform amplitude or it was obvious that the station was not recording correctly at the time of the shot. Then, the amplitude was corrected on the remaining waveforms by taking a single station and gathering waveforms from those stations within 100 meters (42 stations on average). The waveform from the center station was correlated with each of the waveforms from other stations within 100 meters to find the time shift where the two waveforms were most similar. The data were then time shifted by this amount and averaged. This was all done in the frequency band of 4-5 Hz due to the assumption that the waveforms do not change rapidly over the 100-meter radius. For example, the average slowness of the surface waves is around 0.83 s/km and with a frequency of 5 Hz gives a wavelength of 240 meters. The filter used here and all of the filters used in this data analysis were 4-pole, 2-pass (zero phase) Butterworth filters.

We computed an amplitude variation between the new, averaged waveform and the original waveform for the single station using:

$$A_i = \frac{(O(t) \otimes N(t))_{\tau=0}}{(N(t) \otimes N(t))_{\tau=0}} \tag{43}$$

where $O(t)$ is the original waveform, $N(t)$ is the new, averaged waveform, and $\otimes$ represents the non-normalized cross correlation. Dividing the value at zero time lag ($\tau = 0$) for each of the correlations gives the amplitude variation between the two

waveforms (Kendall et al., 2012). We computed these amplitude variations for each station and corrected the original, unfiltered waveform by dividing it by A_i. If the two waveforms were exactly the same, the amplitude variation would be one. The average amplitude correction for Shot #48703 was 1.07 with a standard deviation of 0.32.

In order to test the amplitude correction, we produced synthetic data using filtered Gaussian waveforms with amplitudes similar to our data, actual station positions, and the shot location of Shot #48756 (Figure 17). We inserted amplitude anomalies at 15 of the stations dispersed throughout the array whose amplitudes were three times larger than calculated, and we corrected the amplitudes using the method described. The input slowness was 0.83 s/km, and the resulting average slowness at the highest wave amplitude was 0.83 s/km with a standard deviation over all the cells of 0.0007 s/km. The average calculated azimuth from source to each station was 146.61 degrees with a standard deviation of 3.90 degrees, and the resulting azimuth from wave gradiometry at each station was 146.60 degrees with a 3.90-degree standard deviation. Without the amplitude correction, the average slowness was 0.83 s/km with a standard deviation of 0.0012 s/km, and the average azimuth was 146.60 degrees with a standard deviation of 3.92 degrees. Although the overall change in averages and standard deviations are small, correcting the amplitude this way is essential in minimizing consistent "hot spots" in wave attribute maps associated with individual station problems.

Cell creation and reducing slowness

Gradiometric cells were created around each of the stations that recorded useable data from a shot. The number of stations that yielded acceptable data was usually greater than 350, depending on how many were recording at that time and how many were

discarded because of obvious problems. Each station was a reference station and taking all stations within 50 meters of that reference station created a cell. If the number of stations within 50 meters was less than seven, the closest seven were used. A typical cell, the whole array, and station spacing are shown in Figure 18. The usual assumptions of WG require that the interstation distance be less than 10% of the minimum wavelength in order to compute accurate spatial gradients (Langston, 2007b). Filtering the waveforms in the 4-5 Hz passband and with an average surface wave slowness of 0.83 s/km gives a minimum wavelength of approximately 240 meters, so that the maximum theoretical interstation distance becomes 24 meters. The actual mean distance between a reference station and another station in a cell is 34.8 meters with a standard deviation of 9.9 meters, so the 10% wavelength requirement is not satisfied.

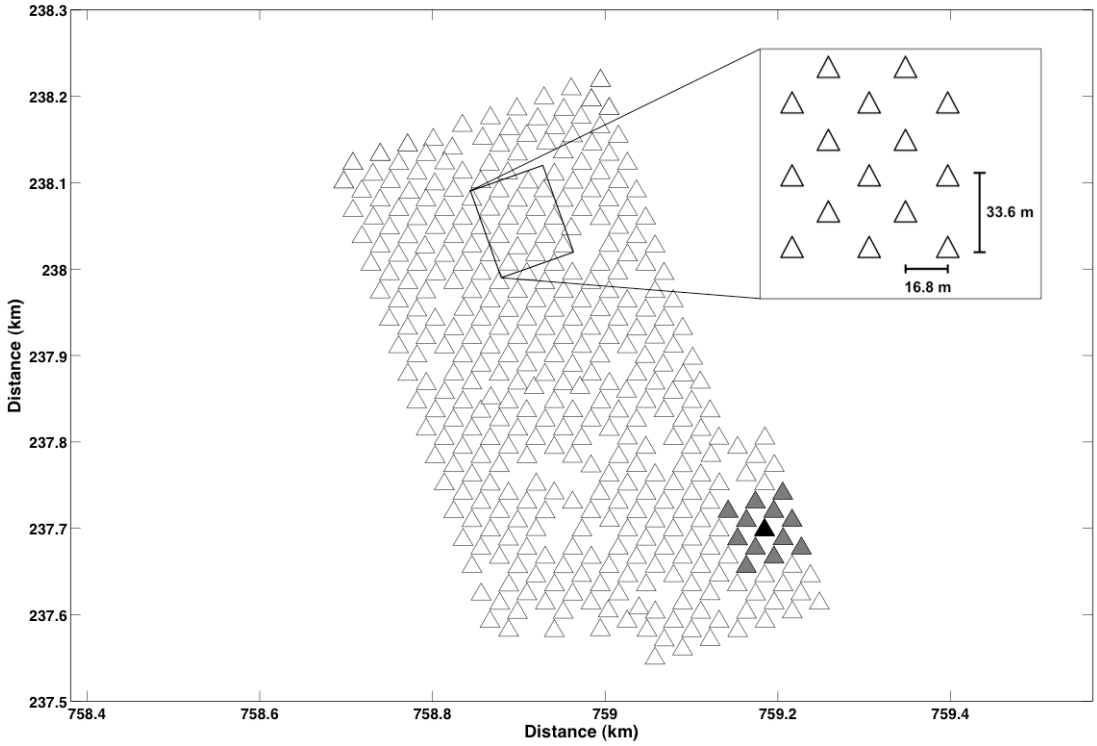

Figure 18: Station and cell configuration
The array geometry is shown with a typical cell filled in with gray and black. Gray triangles represent the outside stations in a cell, and the black triangle is the reference station. Wave gradiometry parameters are calculated using the gray and black stations with output parameters specific to the black triangle position. We used each station in the entire array as a reference station and calculated wave gradiometry parameters for each. Inset is the station geometry. Each of the 23 lines of stations had stations 33.6 meters apart, and the lines were spaced 16.8 meters apart. Because of the staggering of lines, the closest stations were separated by 23.8 meters. The array is approximately 360 by 650 meters in area.

However, we apply a reducing slowness to all stations in a cell relative to the reference station to remedy the wavelength problem under the assumption that the wave field is locally homogeneous (Langston, 2007a; Liang and Langston, 2009). Applying a reducing slowness that is close to the actual slowness time-shifts the waveforms so the phases arrive at each station at theoretically the same time, essentially removing the normal moveout and giving the appearance of infinite (or very large) wave length. The time shift is calculated using a reducing slowness (p_{red}), the relative x and y locations of each station, and an approximate propagation azimuth from the source to that station:

$$t\_shift_i = p_{red}(x_i sin\theta_i + y_i cos\theta_i) \quad . \tag{44}$$

When we calculate the spatial gradient with these slowness-reduced waveforms, the wavelength becomes much greater than before, and the wavelength requirement is satisfied for the spatial gradient calculation. This reducing velocity is removed from the B coefficients after the spatial gradient, A_x, A_y, B_x, and B_y are calculated, so the resulting slownesses reflect the actual slownesses at each reference station location:

$$B_x' = B_x + (p_{red} sin\theta) \tag{45}$$

$$B_y' = B_y + (p_{red} cos\theta) \tag{46}$$

where θ in Equations 45 and 46 is the resulting propagation azimuth calculated from Equation 42. We recalculate this parameter with B_x' and B_y':

$$\theta' = tan^{-1}\left(\frac{B_x'}{B_y'}\right) \quad . \tag{47}$$

The typical processing procedure for a single cell involves applying a reducing velocity, solving for the spatial gradient, using Equations 34 and 35 and the analytic signal method to get A_x, A_y, B_x, and B_y, using Equations 45, 46, and 47 to remove the reducing slowness, and taking an average of the resulting slowness values where the high-amplitude surface wave arrives. This average slowness becomes the new reducing slowness and we repeat this loop until the reducing and the average slownesses are within 0.10 s/km for the surface waves (4-5 Hz) and 0.05 s/km for the body waves (15-25 Hz).

Results

One cell result

As an example of the wave gradiometry analysis, one cell from Shot #48703 is shown in Figure 19. The cell contained 10 stations which are illustrated in gray in the inset map with the center station in black. The data were filtered between 4-5 Hz, and we used a reducing slowness of 0.83 s/km. The top plot is the center-station waveform for the cell, the middle plot is the slowness as a function of time, and the bottom plot is azimuth as a function of time. In the highlighted area, the Rayleigh wave has an average slowness of 0.77 s/km with a standard deviation of 0.03 s/km and an azimuth of 328.01 degrees with a standard deviation of 0.40 degrees. The azimuth is very close to the expected azimuth from source to center station of 327.78 degrees.

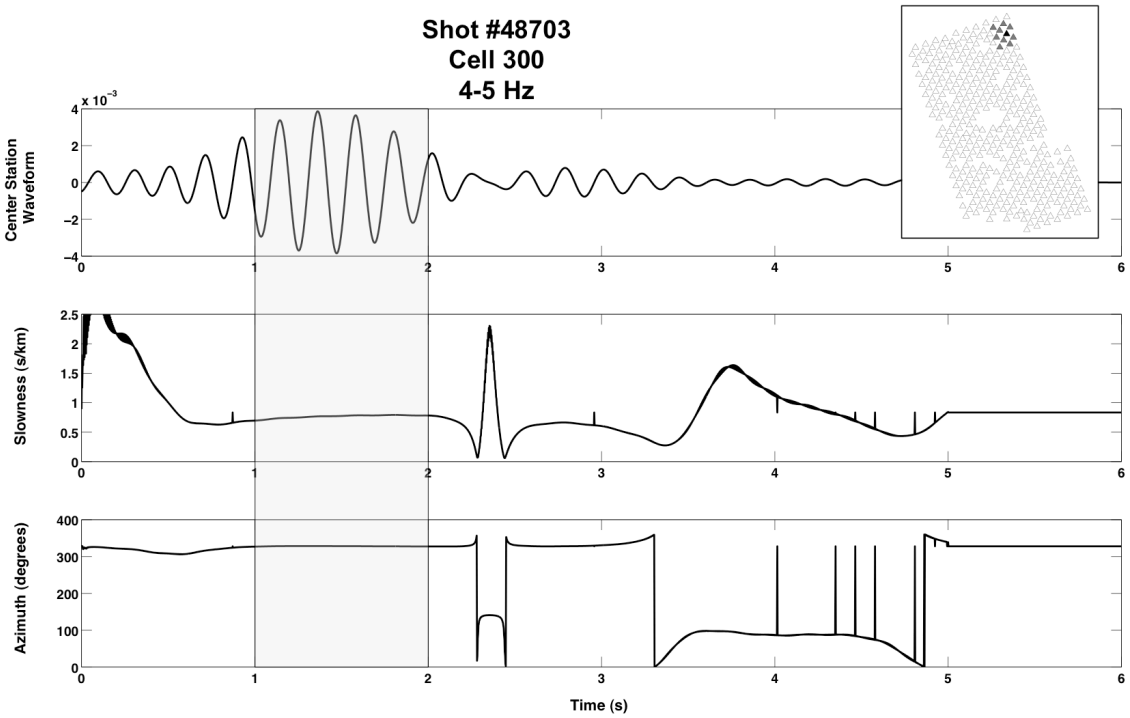

Figure 19: One cell result
Wave gradiometry results from a cell located in the northeast section of the array as shown in the inset map. Gray colored triangles represent outer stations in the cell and the black triangle is the reference station. The top plot is the filtered waveform at the center station, and the bottom two plots of slowness and azimuth are results from using all 10 stations in the array and the wave gradiometry method. The highlighted section from 1-2 seconds is the Rayleigh wave. The slowness and azimuth estimates for that one second band are 0.77 s/km with a standard deviation of 0.03 s/km and 328.01 degrees with a standard deviation of 0.40 degrees.

The estimates in this low frequency band give us smoothly-varying results for high-amplitude waves. When the wave amplitude is low or there may be more than one wave arriving at a time, the slowness and azimuth results are not smoothly varying, for example between the Rayleigh wave and coda at about 2.4 seconds. This is due to temporal discontinuities in the analytic signal we use to solve for our A and B coefficients (Langston, 2007c).

Quiver plots

For each of the 359 cells for Shot #48703 there are slowness and azimuth estimates, and we display these data by representing the normalized wave amplitude at each station as shaded contours. Plotted on top of the filtered wave amplitudes are slowness-azimuth vectors for each of the cells. These vectors point in the propagation azimuth of the waves and have a length corresponding to the slowness at that cell. Figure 20 shows two of these plots: one filtered at 4-5 Hz to target the surface waves and normalized by the largest surface wave amplitude and the other filtered at 15-25 Hz to target the body waves and normalized by the largest body wave amplitude. All of the waves filtered 4-5 Hz in this study employed a reducing slowness of 0.83 s/km, and those filtered 15-25 Hz used a reducing slowness of 0.27 s/km.

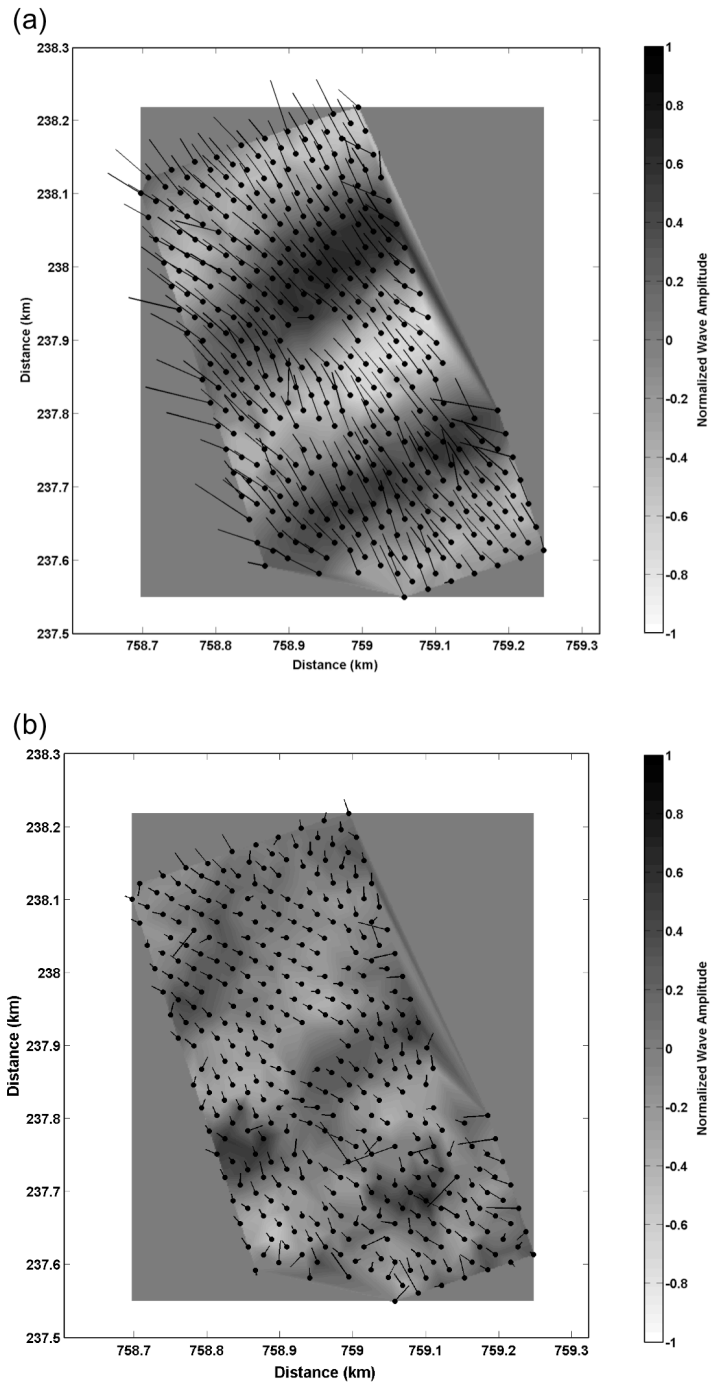

Figure 20: Quiver plots
Wave parameters from Shot #48703 at 1.5 seconds filtered 4-5 Hz (a) and at 0.45 seconds filtered at 15-25 Hz (b). The gray coloring represents the normalized wave amplitude at each cell. The circles are at the center station for each cell, and the lines from each circle are slowness-azimuth vectors. The direction they are pointing is in the direction of the wave propagation, and the length of the lines corresponds to slowness. The longer the lines are, the slower the wave is traveling at that point.

The body waves in Figure 20b are noticeably less correlated along wave crests and troughs compared to the surface waves in Figure 20a. Because the waves scatter as they travel across the array, some low-amplitude regions as well as wave interference areas are present and we, therefore, observe anomalous features such as uncharacteristic azimuth changes and large slownesses. These are caused by similar effects that are present in Figure 19 at 2.4 seconds and should be interpreted as an indicator of wave interference and not as a processing artifact. The wave parameters that represent wave characteristics largely uncontaminated from interfering waves are those in a time band where the waves are high amplitude and there is no interference.

WG compared to FK

We followed a wave crest from its initial entrance into the array to its exit to get a representation of phase slowness for high amplitude waves in both frequency bands. This was straightforward to do with the surface waves in the 4-5 Hz band as they did not lose much amplitude as they traveled across the array. It was more difficult to do with the body waves in the 15-25 Hz band since they scattered and lost amplitude across the array. Creating a standard shot gather helped us to estimate the arrival time and time window for particular arrivals when picking the wave crest. Once we had the time of the wave crest arrival at each cell for both frequency bands, we averaged the slowness and azimuth values for approximately one wavelength around the peak which was about 50 points (0.1 seconds with a 0.002-second sampling rate) on either side of the surface wave peak and 10 points (0.02 seconds) on either side of the body wave peak.

We divided the array in half and averaged all of the slowness values in each half and compared these values against frequency-wavenumber (Nawab et al., 1985) slowness

results for the same stations. To be systematic, we will present wave gradiometry results from three representative shots (all shown in Figure 17): one southwest (47918) at an average of 2.28 km from the stations, one northwest (48756) at 1.53 km, and one southeast (48703) of the array at 1.17 km and in two frequency bands: 4-5 Hz and 15-25 Hz. These results are shown in Figure 21.

The range around the WG average is calculated using the standard deviation of all the averages, and the range around the frequency-wavenumber peak power is calculated by taking the values out to 50% peak power. The synthetic array responses for the top and bottom portions of the array show that a slowness range is introduced purely because of the array aperture. This range is approximately 0.051 s/km for the top half of the array in the 15-25 Hz passband, 0.056 s/km for the bottom half, 0.223 s/km for the top half of the array in 4-5 Hz band, and 0.219 s/km for the bottom half in that band. All resulting FK ranges are greater than these array response ranges.

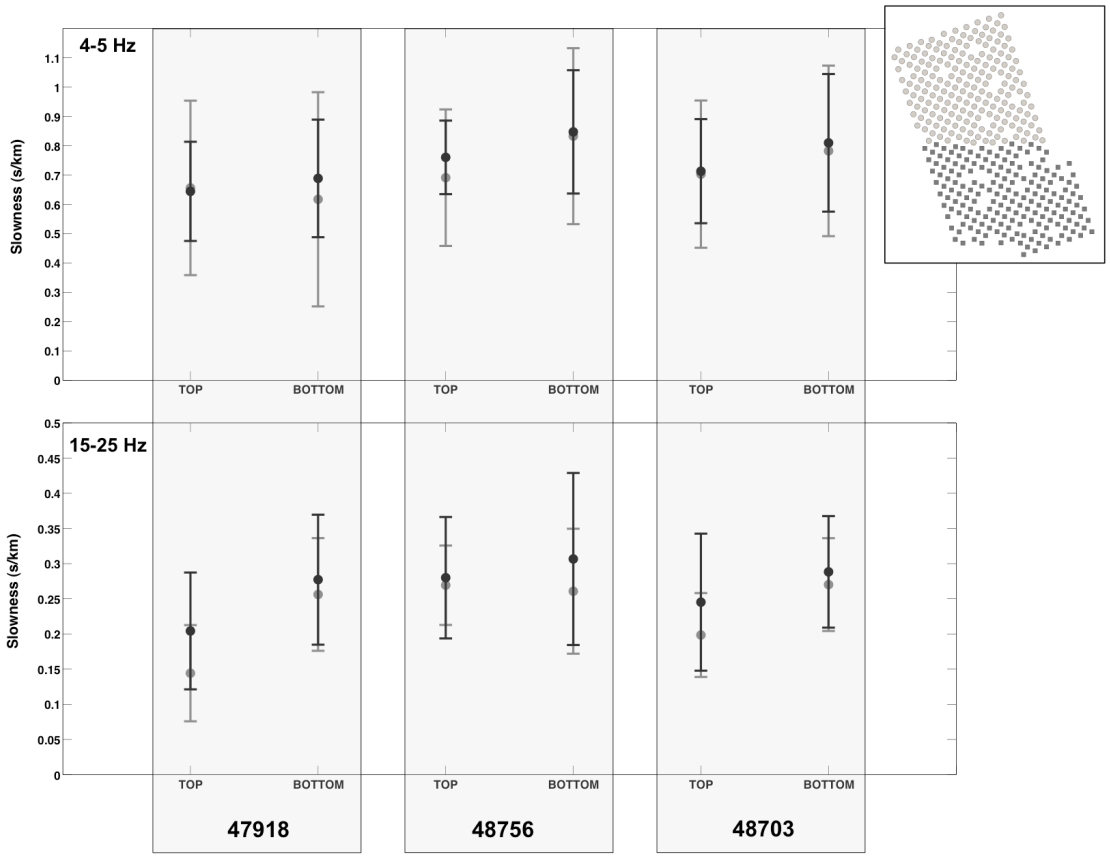

Figure 21: Azimuth results, WG compared to FK
Phase velocity results averaged over two halves of the array for Shots #47918, 48756, and 48703. The inset map shows how the array was divided in half; each half is approximately 325 meters from top to bottom. The top plot is phase velocities in the 4-5 Hz region where the black circles and range bars are for the gradiometry average and standard deviation results, and the gray circles and range bars are the FK peak and range out to half the peak power. The bottom plot is for 15-25 Hz range, so it is showing body-wave phase velocities. Notice that the two scales are different: the top scale is larger because the surface waves are slower.

The wave gradiometry average and frequency-wavenumber peak power results in both frequency bands are relatively close, but they all have large ranges around the peak indicating that the waves are being scattered before they enter the array and while they travel through the array. The minimum wavelength for a surface wave phase traveling at 0.83 s/km and a maximum frequency of 5 Hz is 240 meters. Each half of the array is approximately 325 meters in length, so the surface wave should not be changing significantly over that distance. The minimum body wave wavelength is about 150 meters (slowness of 0.27 s/km and maximum frequency of 25 Hz), so it is changing slightly more over half of the array but should not be dramatically changing as only two horizontal wavelengths can propagate in that distance.

We analyzed wave azimuth estimates for the whole array to examine the full spatial dispersion in both frequency bands. The array response for the whole array is azimuthally dependent. If the energy is coming from 0-90 or 180-270 degrees, the range due to array configuration is 7.33 degrees in the 15-25 Hz passband and 11.31 in the 4-5 Hz band. If the energy is coming from 90-180 or 270-360 degrees, the range is 16.39 degrees for 15-25 Hz and 23.06 for 4-5 Hz. Figure 22 shows the azimuth results for each shot. The calculated azimuth range from the sources to each receiver is shown on the plots as horizontal boxes, and the estimated azimuth range is determined using the standard deviation for WG and values out to 50% peak power for FK. The azimuth results for both wave gradiometry and FK in the two frequency bands have good agreement with the calculated azimuth range, but the ranges are quite high for relatively close shot-distances. This is more evidence for a high amount of wave scattering in the array region.

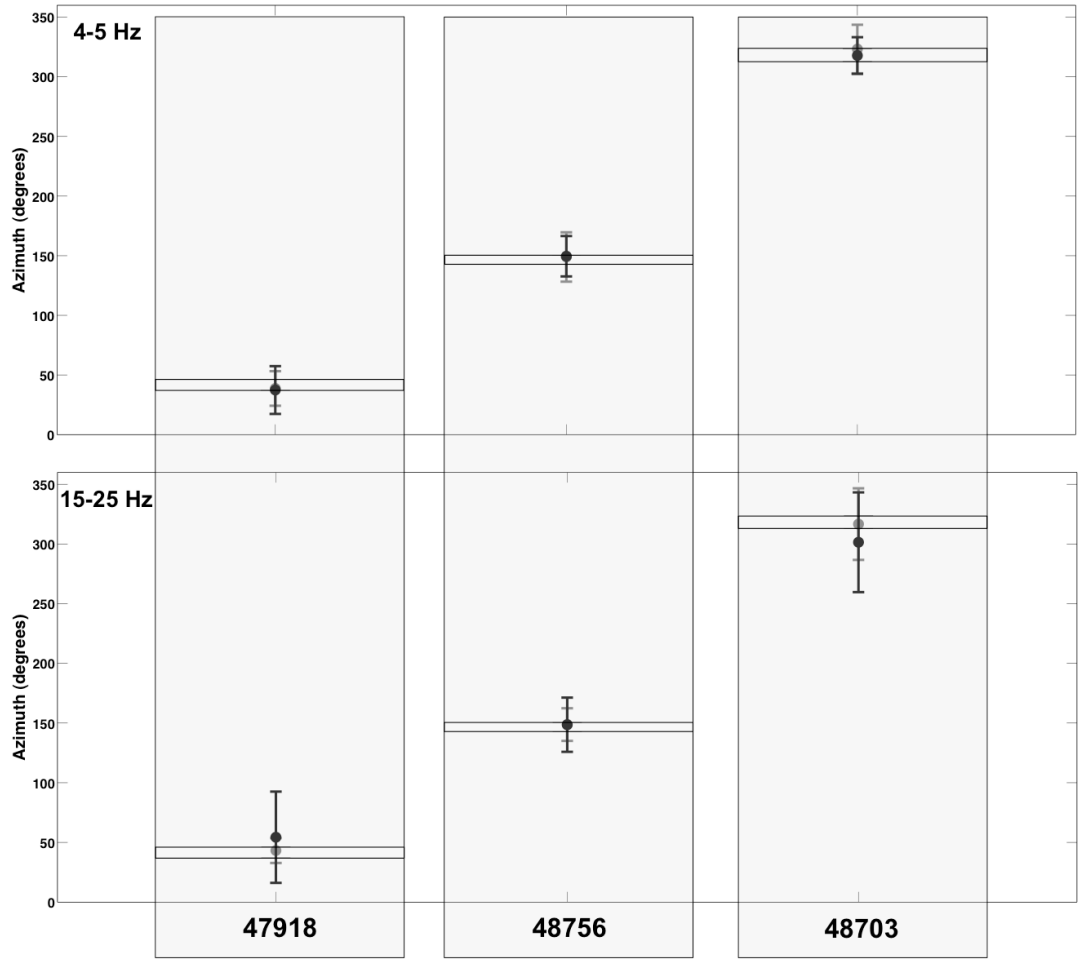

Figure 22: Azimuth results, WG compared to FK
Azimuth results for the whole array for Shots #47918, 48756 and 48703. The top plot is filtered 4-5 Hz to target surface waves, and the bottom plot is filtered 15-25 Hz to target the body waves. Horizontal boxes in each vertical box represent calculated azimuthal ranges from shot location to each station location. The black circles and range bars are wave-gradiometry results, and the gray circles and range bars are frequency-wavenumber results. The circle for the wave gradiometry represents the average of all of the azimuth results from the cells, and the circle for the FK is the azimuth at peak power. The range bars for wave gradiometry were calculated by taking the standard deviation of all of the azimuth results at all of the cells. The FK range bars were calculated using the azimuth range out to 50% power.

Phase velocity maps

The goal of having shots at varying azimuths around the array was to construct an overall phase velocity map that could help us determine mined/unmined structure under the array. We created these by plotting each slowness value obtained from averaging over a wavelength around a wave crest and contouring the results to create a seamless map. A representative sample of these phase velocity maps are shown in Figure 23. The three rows represent similar-azimuth shots. Each same-azimuth shot is within 260 meters of its counterpart. Generally, there are similarities in the maps from the same azimuth, but they are quite different across different azimuths. Shots #47918 and 47916 have almost-vertical trends of slower and faster bands; on the right half of the array a faster band is visible closer to the middle, and a slower band is visible closer to the edge. Shots #48756 and 48766 show more horizontal trends and both show a slow line of cells at the bottom third of the array. Shots #48703 and 48664 also have a slow patch at the bottom third but this is noticeably more north in the array. These maps are similar from the same azimuths but different from dissimilar azimuths indicating that the changes in maps are most likely due to wave scattering effects along different wavepaths and not due to processing errors or biases.

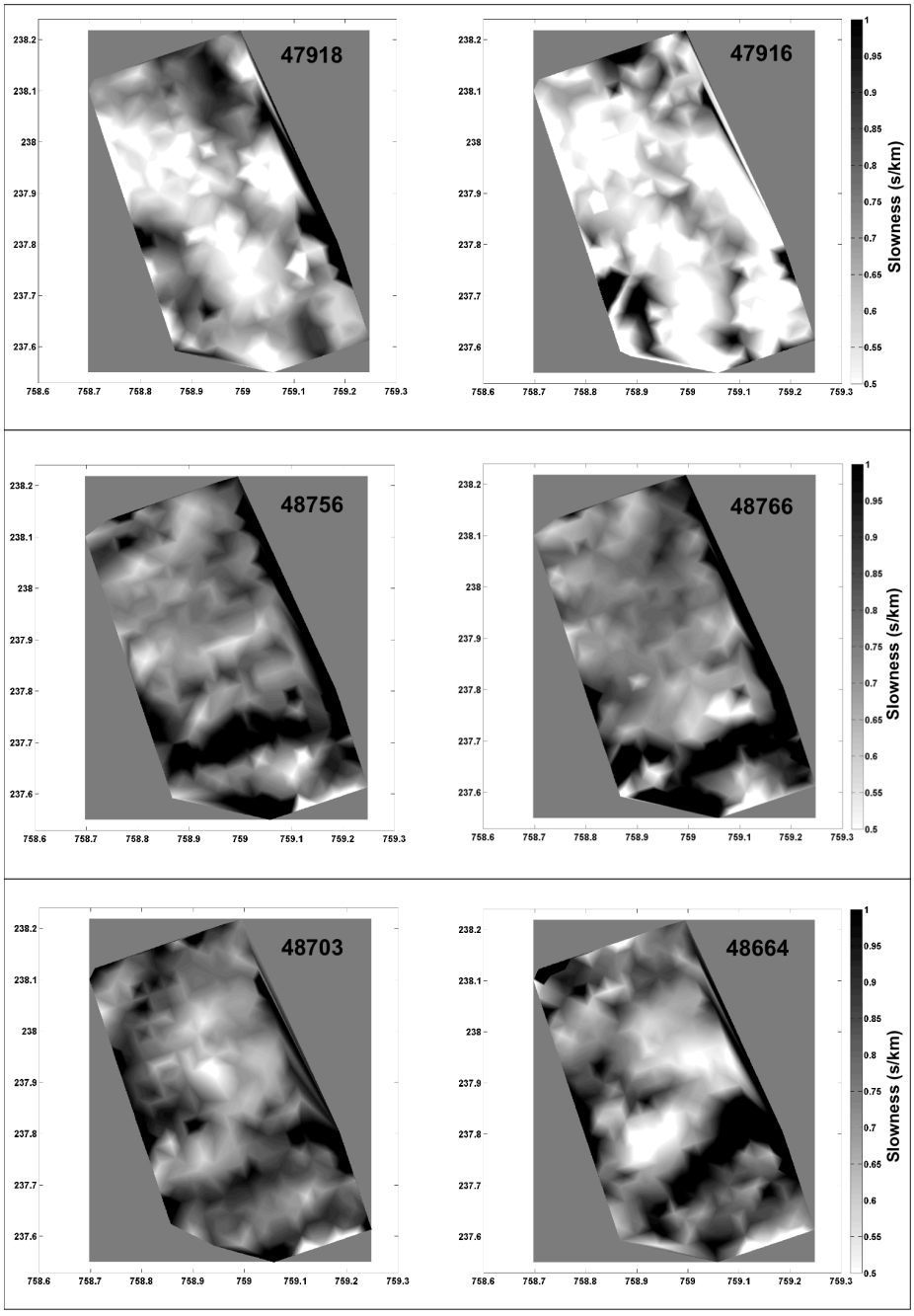

Figure 23: Phase velocity maps
Phase velocity maps for three groups of similar-azimuth shots all done in a 4-5-Hz band. The first row of plots are for shots southwest of the array, the second row are for shots northwest of the array, and the bottom row are southeast of the array. Groups of similar-azimuth shots are within 260 meters of each other. The slowness grayscale bars for all shots are the same: a minimum of 0.5 s/km and a maximum of 1.0 s/km. Notice how the similar-azimuth shots are relatively alike, and how unlike the maps are for different azimuth groups.

Discussion

To test WG methods with high-frequency sources and confirm that the large azimuth and slowness ranges we see in the data are not processing errors, we employ SPECFEM3D and its internal mesher to create synthetic data. SPECFEM3D simulates three-dimensional, elastic wave propagation using the spectral element method (SEM) to solve the equations of motion (Tromp et al., 2008).

The mesh setup is shown in Figure 24. The P-wave velocity model was an idealized model given from an available well log from Global Geophysical Services and the S-wave, attenuation, and density were calculated based on equations for sediments using relations presented by Brocher (2005; 2008). To simulate the coal-mined and solid-coal areas in our region, we inserted a large low-velocity layer at 25-125 meters depth that spanned the whole 4 km area except for a high-velocity layer that was placed under our station array (Figure 24). Figure 25 shows the WG phase velocity estimates for the peak amplitude of the synthetic data at each cell in the frequency range of 2-3 Hz. The box shows where the high-velocity region occurs in the input mesh. These parameters vary smoothly across the array even though there are high-impedance contrasts. The low-slowness region in the box agrees well with the input slowness of 0.3 s/km (3.8 km/s), and the region south of the box agrees with the low-velocity region of the mesh with a slowness of approximately 0.4 s/km (2.5 km/s). However, it is interesting to note that the region at the north end of the array does not agree with the slowness input of the mesh indicating that the surface wave is still affected by the low velocity layer at depth when close to the low velocity/high velocity boundary in the north. This wavelength-dependent effect is a reasonable consequence of wave propagation in a relatively simple

model but does not explain the high variability in wave attributes seen in the field data. The high variability observed from waves propagating along different paths in different directions must mean that the Earth is quite heterogeneous all along wave paths. The accurate characterization of this heterogeneity will need information within the array and also outside of the array. It seems that velocity heterogeneity along wave paths has effectively spoiled our original hypothesis that maps of wave attributes will allow a direct empirical look at the structure under the array to detect possible mined areas.

Waves are obviously highly scattered in the area of our array, and we examine the coda to further confirm the nature of the scattering. Figure 26 shows frequency-wavenumber analysis of the last 2 seconds (48703) and 3 seconds (47918 and 48756) of waveform data from the shots. FK analysis on Shot #47918 shows that the waves are coming in from all directions with a variety of slownesses. The expected azimuth is 221.66 degrees, but most of the energy seems to be coming from about 180 and 350 degrees signifying scattered waves. Shot #48756 also shows arrivals from a large variety of azimuths traveling with a wide range of slownesses. The expected azimuth for this shot is 326.53 degrees where a considerable amount of energy is concentrated, but an even larger amount seems to be backscattered from about 180 degrees away from the source azimuth. FK analysis on Shot #48703 shows two distinct bands of azimuths. The expected direction is 138.22 degrees, and a large amount of energy seems to be backscattered from this shot as well.

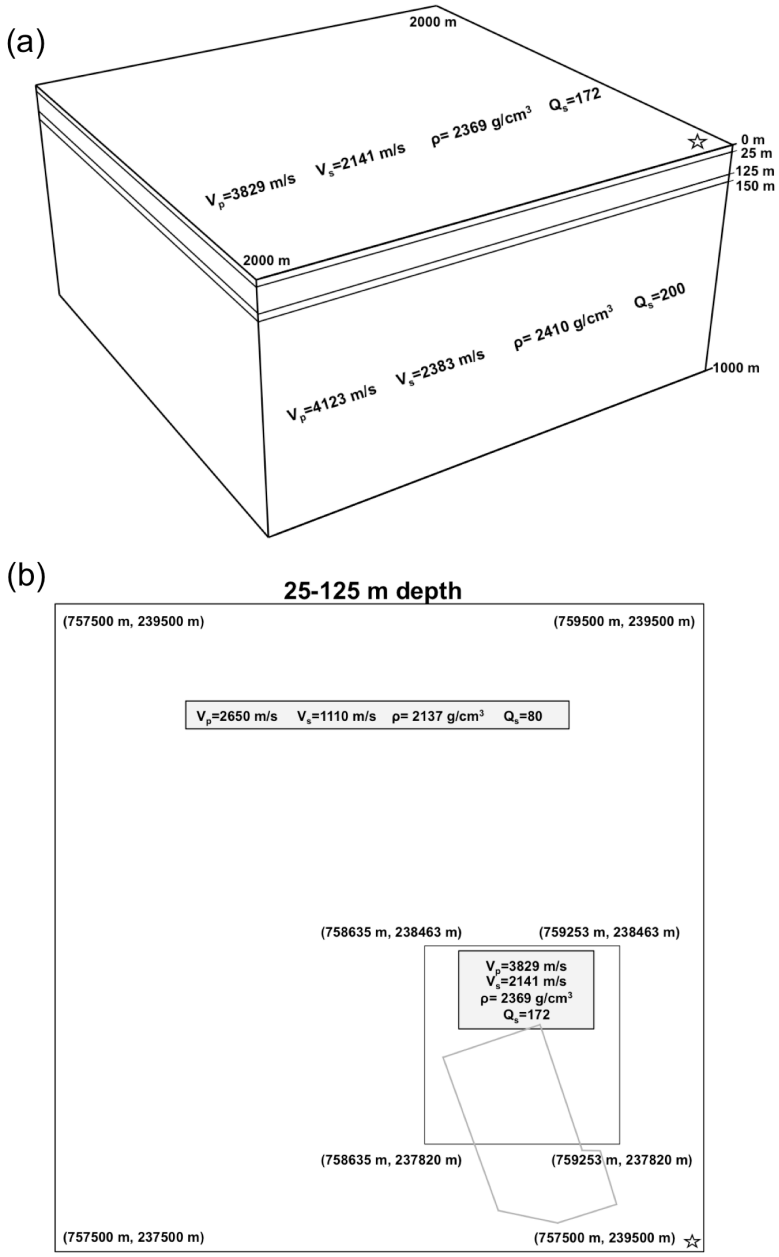

Figure 24: Mesh configuration
Details of the mesh used with SPECFEM3D to create synthetic data. The top figure (a) is the side view of the mesh. It was 2 km by 2 km and 1 km deep. The P-wave velocity, S-wave velocity, density, and quality factor are all listed for the two layers visible. The bottom plot figure (b) shows the parameters for the 25-125 meter depth region. That slice of the mesh is low velocity to simulate coal mines except for an area right below and north of the array which is high velocity and represents unmined coal. The array is shown outlined in gray in the bottom-right corner of (b).

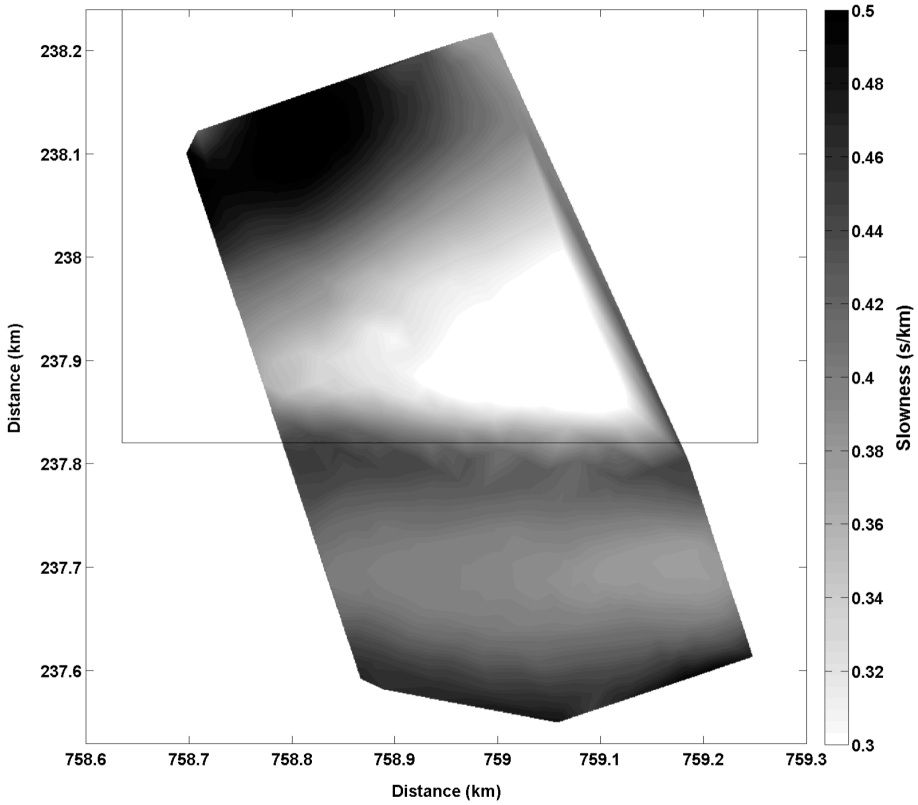

Figure 25: Synthetic phase velocity map
Phase velocity map for synthetic data filtered 2-3 Hz. The slowness colorbar has a minimum of 0.3 s/km and a maximum of 0.5 s/km. The black box on the top half of the map represents the high-velocity region from 25-125 meters depth.

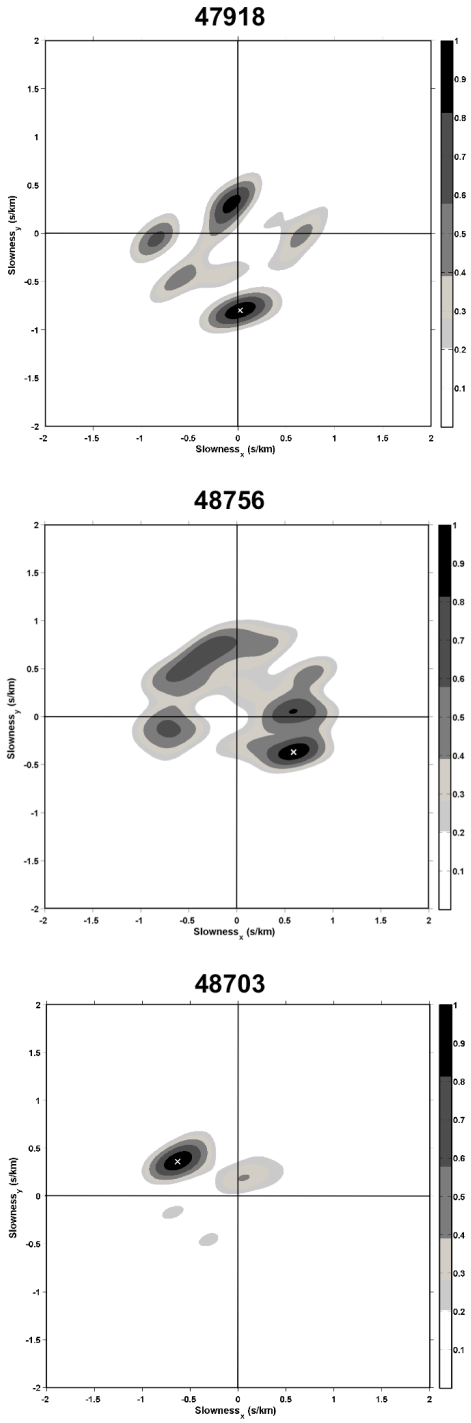

Figure 26: FK analysis of coda waves
FK analysis or the coda arriving at the last 2-3 seconds of the 6-second trace for the 4-5-Hz band. The expected direction of Shot #47918 is in the third quadrant, 48756 is in the fourth quadrant, and 48703 is in the second quadrant. The shades of gray represent power where the highest power represents a direction and slowness that most agrees with the waves.

Langston et al. (2009) found similar scattering results for a wave gradiometry experiment with near-proximity sources. The experiment was done in a mountainous river valley with large topography changes over short distances. Although they only had one gradiometer cell and two shots, they found that the wavefield in that close range was very complex and produced different wave parameter results for the two shots. Their wave gradiometry results agreed well with frequency-wavenumber results indicating that the fast-changing wave parameters are true representations of the wavefield. An analysis of the coda reveals that the waves propagate in all directions: back and forth across the valley and even back towards the source. This further drove the point of large-scale heterogeneities in the region. The wavelength of their waves allowed several wavelengths to propagate from the source before the waves reached their receivers. The wavelength of our waves in this experiment are about 240-300 meters (0.83 s/km and filtered 4-5 Hz) and 150-246 meters (0.27 s/km and filtered 15-25 Hz), so many seismic-wavelengths could propagate in the range of 314-2677 meters from shot to station. The waves propagating through the extensively mined region throughout the area are highly scattered and reminiscent of scattering seen by Langston et al. (2009).

WG is based on the assumption that there is one single propagating wave from source to receiver (Langston, 2007a). In a complicated structure that we have, that is most likely not the case. The theory essentially still works, but if two waves are interfering, the resulting wave gradiometry parameters have anomalies at the interference time (Langston, 2007c), and if two waves beat together, the resulting wave gradiometry parameters are a function of the signal-to-noise ratio (SNR) of the two waves (Langston,

2007a). If two waves arrive at a station at the same time with different phase velocities, the resultant A and B parameters will be:

$$A \cong A_1 + A_2\, SNR^{-1}$$
$$B \cong B_1 + B_2\, SNR^{-1} \quad (48)$$

where A_1 and B_1 are the A and B parameters of the higher-amplitude wave and A_2 and B_2 are the A and B parameters of the lower-amplitude wave in the signal. If the signal-to-noise ratio of both waves is the same, the resulting A and B parameters will be the sum of the two single wave parameters. On the other hand, if the signal-to-noise ratio of the lower-amplitude wave is relatively small, it will not affect the A and B parameters dramatically, but it will still alter the slowness and azimuth results we obtain for that wave. We conclude that this beating effect is causing the changes in our wave parameters with azimuthally-varying sources.

Conclusion

Dynamite sources created a complicated wavefield in the coal mined area of Belmont County in eastern Ohio. Twenty-nine sources from differing azimuths around a 376-station array showed varied slowness estimates for consistent station positions preventing us from inferring information about the mine-created structure under the array, and, instead, turning to find out the reason behind the slowness differences. Wave scattering caused wave interference that was visible in the wave attribute results as anomalous spikes in wave slowness, and beat patterns across the array. Azimuth estimates from the array were consistent with predicted azimuths from shot to stations,

but the variance in the estimates was quite large. This, again, was caused by wave scattering by propagation in heterogeneous media.

A synthetic test was employed to determine whether the variation in wavefield parameters was a real effect or a processing artifact, and the slowness results showed that the wavefield was smoothly varying for the same station and shot configuration as the actual experiment. The synthetic waves propagated through a large impedance contrast in the middle of the array, and this is visible in the wave attributes. In the actual data, the velocity variations must be larger and much more abundant to create the scattering results that we see.

Despite the varying wavefield parameters, we show that it is possible to conduct seismic-wave gradiometry with high-frequency sources close to the array, but the results should be critically interpreted as the wave attributes could be a function of many waves instead of one. For future experiments, it is suggested that the geometrical spreading and radiation pattern estimates be interpreted as well to give more clues on the nature of wave scattering and interference. Future experiments should also use an array configuration that includes sources within the array in order to observe the waves as they begin to interfere as they travel out from the source.

References

Brocher, T. M., 2005, Empirical relations between elastic wavespeeds and density in the Earth's crust: Bulletin of the Seismological Society of America, **95**, no. 6, 2081-2092.

Borcher, T. M., 2008, Compressional and shear-wave velocity versus depth relations for common rock types in northern California: Bulletin of the Seismological Society of America, **98**, no. 2, 950-968.

Daniels, J., 1988, Locating caves, tunnels, and mines: Geophysics: The Leading Edge of Exploration, **7**, no. 3, 32-52.

Kendall, L. M., C.A. Langston, W. H. K. Lee, C. J. Lin, and C. C. Liu, 2012, Comparison of point and array-computed rotations for the TAIGER explosions of 4 March 2008: Journal of Seismology, doi:10.1007/s10950-012-9297-4.

Langston, C. A., 2007a, Spatial gradient analysis for linear seismic arrays: Bulletin of the Seismological Society of America, **97**, no. 1B, 265-280.

Langston, C. A., 2007b, Wave gradiometry in two dimensions: Bulletin of the Seismological Society of America, **97**, no. 2, 401-416.

Langston, C. A., 2007c, Wave gradiometry in the time domain: Bulletin of the Seismological Society of America, **97**, no. 3, 926-933.

Langston, C., W. H. K. Lee, C. J. Lin, and C. C. Liu, 2009, Seismic-wave strain, rotation, and gradiometry for the 4 March 2008 TAIGER explosions: Bulletin of the Seismological Society of America, **99**, no. 2b, 1287-1301.

Liang, C., and C. A. Langston, 2009, Wave gradiometry for USArray: Rayleigh waves: Journal of Geophysical Research, **114**, doi:10.1029/2008JB005918.

Naweb, S., F. Dowla, and R. Lacoss, 1985, Direction determination of wideband signals: IEEE Transactions on Acoustics, Speech, and Signal Processing, **33**, no. 5, 1114-1122.

Ohio Division of Geological Survey, 2006, Bedrock geologic map of Ohio: Ohio department of Natural Resources, Division of Geological Survey Map BG-1, generalized page-size version with text, 2p., scale 1: 2,000,000.

Tromp, J., D. Komatitsch, and Q. Liu, 2008, Spectral-element and adjoint methods in seismology: Communications in Computational Physics, **3**, no. 1, 1-32.

CHAPTER 5

CONCLUSIONS

We have investigated three unique datasets to show how spatial gradient analysis and seismic-wave gradiometry can be applied to help us learn about the wave field and explore how the waves travel from one point to another. These datasets have solidified that wave gradiometry can be used in high-frequency settings and that the technique is possible with off-the-shelf geophones. Future studies with wave gradiometry should investigate if the data analysis tool can be applied to high-frequency datasets in less velocity-heterogeneous areas to directly determine the properties of structure under the array.

Comparison of Point and Array-Computed Rotations for the TAIGER Explosions of 4 March 2008

Acceleration-derived geodetic rotation rates and point rotation rate data recorded by Eentec R-1 rotational seismometers after two large explosions in northeastern Taiwan were successfully compared. Computed array rotation rate showed little variation over the five array stations, consistent with long-wavelength seismic wave propagation. The absolute value of the normalized cross-correlation values between the two sets of rotational waveforms in the frequency band 3–5 Hz had an average of 0.84. Spectral analysis showed that the spectral ratios varied by component and often had large resonance peaks near 4.0–4.3 Hz. The *x* components of two stations (N06 and N09) were particularly problematical. Variations in the observed point rotation rate data are attributed to variations in instrument response and not site heterogeneity.

Small-Scale Array Experiments in Seismic-Wave Gradiometry

Horizontal slowness and propagation azimuth from two, two-dimensional dense seismic-arrays agreed with results from a linear refraction line and with expected values. Slowness-azimuth vectors from Experiment 2 clarify wavefield visualization, and the location abilities prove possible and increasingly more accurate with an increase in gradiometric cells around the source. Scatter plots from Experiment 3 clearly illustrated the decrease in slowness and azimuth range with the increase in center stations. A drawback of this technique, as shown in the huddle test, is that the results are sensitive to uncalibrated instruments. The experiments have shown that seismic-wave gradiometry is reliable with off-the-shelf geophones and it produces good results for dense, small-scale datasets.

Seismic-Wave Gradiometry with a Dense, 2D Array

Dynamite sources created a complicated wavefield in the coal mined area of Belmont County in eastern Ohio. Twenty-nine sources from differing azimuths around a 376-station array showed varied slowness estimates for consistent station positions preventing us from inferring information about the mine-produced structure under the array, and, instead, leading us to find out the reason behind the slowness differences. Wave scattering caused wave interference that was visible in the wave attribute results as anomalous spikes in wave slowness, and beat patterns across the array. Azimuth estimates from the array were consistent with predicted azimuths from shot to stations, but the variance in the estimates was quite large. This, again, was caused by wave scattering by propagation in heterogeneous media.

Despite the varying wavefield parameters, we show that it is possible to conduct seismic-wave gradiometry with high-frequency sources close to the array, but the results should be critically interpreted as the wave attributes could be a function of many waves instead of one. For future experiments, it is suggested that the geometrical spreading and radiation pattern estimates be interpreted as well to give more clues on the nature of wave scattering and interference. Future experiments should also use an array configuration that includes sources within the array in order to observe the waves as they begin to interfere as they travel out from the source.

References

Grant, E. B. (2010). Gladwin tensor strainmeter calibration using seismic data: instrument calibration methods and wave gradiometry applications. Ph.D. dissertation, The University of Memphis, Memphis, Tennessee, 216 pp.

Langston, C. A. (2007a). Spatial gradient analysis for linear seismic arrays, Bulletin of the Seismological Society of America **97**, no. 1B, 265-280.

Langston, C. A. (2007b). Wave gradiometry in two dimensions, Bulletin of the Seismological Society of America **97**, no. 2, 401-416.

Langston, C. A. (2007c). Wave gradiometry in the time domain, Bulletin of the Seismological Society of America **97**, no. 3, 926-933.

Langston, C., W. H. K. Lee, C. J. Lin, and C. C. Liu (2009). Seismic-wave strain, rotation, and gradiometry for the 4 March 2008 TAIGER explosions, Bulletin of the Seismological Society of America **99**, no. 2b, 1287-1301.

Langston, C. and C. Liang (2008). Gradiometry for polarized seismic waves, Journal of Geophysical Research **113**, doi:10.1029/2007JB005486.

Liang, C., and C. A. Langston (2009). Wave gradiometry for USArray: Rayleigh waves, Journal of Geophysical Research **114**, doi:10.1029/2008JB005918.

Spudich, P., L. K. Steck, M. Hellweg, J. B. Fletcher, and L. M. Baker (1995). Transient stresses at Parkfield, California produced by the M 7.4 Landers earthquake of June 28, 1992: observations from the UPSAR dense seismograph array, Journal of Geophysical Research **100**, 675-690.